SAND2021-12610

SANDIA REPORT

Printed September, 2021

Sandia National Laboratories

Optical Imaging on Z LDRD: Design and Development of Self-Emission and Debris Imagers

D. A. Yager-Elorriaga (1683), M. M. Montoya (1659), D. E. Bliss (1659), C. R. Ball (1691), P. Atencio (1692), B. C. Carpenter (1536), K. Fuerschbach (6783), K. W. Fulford (1659, UNM), D. C. Lamppa (1659), M. C. Lowinske (1692), L. Lucero (1659), A. J. Maurer (1692), S. Patel (1659), A. Romero (1646), D. J. Scoglietti (1659), A. Tanbakuchi (1535), and A. J. York (1681)

Prepared by
Sandia National Laboratories
Albuquerque, New Mexico 87185
Livermore, California 94550

Issued by Sandia National Laboratories, operated for the United States Department of Energy by National Technology & Engineering Solutions of Sandia, LLC.

Available to DOE and DOE contractors from

U.S. Department of Energy
Office of Scientific and Technical Information
P.O. Box 62
Oak Ridge, TN 37831

Telephone: (865) 576-8401
Facsimile: (865) 576-5728
E-Mail: reports@osti.gov
Online ordering: http://www.osti.gov/scitech

Available to the public from

U.S. Department of Commerce
National Technical Information Service
5301 Shawnee Road
Alexandria, VA 22312

Telephone: (800) 553-6847
Facsimile: (703) 605-6900
E-Mail: orders@ntis.gov
Online order: https://classic.ntis.gov/help/order-methods

ABSTRACT

We present an overview of the design and development of optical self-emission and debris imaging diagnostics for the Z Machine at Sandia National Laboratories. These diagnostics were designed and implemented to address several gaps in our understanding of visibly emitting phenomenon on Z and the post-shot debris environment.

Optical emission arises from plasmas that form on the transmission line that delivers energy to Z loads and on the Z targets themselves; however, the dynamics of these plasmas are difficult to assess without imaging data. Addressing this, we developed a new optical imager called SEGOI (Self-Emission Gated Optical Imager) that leverages the eight gated optical imagers and two streak cameras of the Z Line VISAR system. SEGOI is a low cost, side-on imager with a 1 cm field of view and 30-50 μm spatial resolution, sensitive to green light (540-600 nm). This report outlines the design considerations and development of this diagnostic and presents an overview of the first diagnostic data acquired from four experimental campaigns. SEGOI was fielded on power flow experiments to image plasmas forming on and between transmission lines, on an inertial confinement fusion experiment called the Dynamic Screw Pinch to image low density plasmas forming on return current posts, on an experiment designed to measure the magneto Rayleigh-Taylor instability to image the instability bubble trajectory and self-emission structures, and finally on a Magnetized Liner Inertial Fusion (MagLIF) experiment to image the emission from the target.

The second diagnostic developed, called DINGOZ (Debris ImagiNG on Z), was designed to improve our understanding of the post-shot debris environment. DINGOZ is an air-tight enclosure that houses electronics and batteries to operate a high-speed (10-400 kfps) camera in the Z Machine center section. We report on the design considerations of this new diagnostic and present the first high-speed imaging data of the post-shot debris environment on Z.

FUNDING ACKNOWLEDGMENT

This work was funded jointly by Keith Matzen via a Strategic Partnership and the Assured Survivability and Agility with Pulsed Power (ASAP) Mission Campaign under LDRD Project Number 219690, titled "Self-Emission Optical Imagers on Z."

CONTENTS

LIST OF FIGURES

LIST OF TABLES

NOMENCLATURE

Table 0-1. List of acronyms used thorughout this report.

Abbreviation	Definition
LOS	Line of Sight
FOV	Field of View
VISAR	Velocity Interferometer System for Any Reflector
ZLV	Z Line VISAR
SEGOI	Self-Emission Gated Optical Imager
DINGOZ	Debris Imaging on Z
DToF	Debris Time of Flight
DSP	Dynamic Screw Pinch
MagLIF	Magnetized Liner Inertial Fusion
ICF	Inertial Confinement Fusion
MRT	Magneto Rayleigh-Taylor
FIZ	Fiber Imaging on Z
MITL	Magnetically Insulated Transmission Line

1. INTRODUCTION

The Z Machine at Sandia National Laboratories is the world's largest pulsed power facility.[1] Electrical energy is compressed in space and time to deliver enormous current densities and magnetic pressures that are used for a variety of applications, including the pursuit of multi-MJ yields of nuclear fusion energy for stockpile stewardship applications, the generation of the world's most powerful x-ray source for radiation effects sciences, the study of materials under high energy density conditions important for the safety and reliability of our nuclear stockpile, and improving our understanding of the fundamental science of astrophysical systems. Most of these applications involve generating matter in the high energy density regime, where pressures exceed 1 Mbar (roughly the internal energy density of a hydrogen molecule). As such, many of the diagnostics on Z are focused on measuring the properties of x-rays and neutrons produced from such intense conditions. A notable gap in our diagnostic suite is the ability to image optical phenomenon, particularly that of low density plasmas. These plasmas form on power flow surfaces in the transmission line that delivers energy to the various Z loads in addition to Z targets themselves. The purpose of this LDRD is to address this gap by developing optical imaging diagnostics relevant to the many important applications pursued on the Z Machine.

Similar to power flow plasmas, the post-shot debris environment is important for all Z experiments. Megajoules of energy are delivered to centimeter-scale loads, ultimately causing the targets along with nearby load hardware to explode. This debris is responsible for damaging diagnostics, radiation effects sciences sample cassettes, and the insulator stack. Furthermore, understanding how this debris scales with energy delivered is critical for the design of a next generation pulsed power facility. Based on Debris Time of Flight (DToF) accelerometer signals, the debris is thought to consist of four stages, including (1) hot plasma, (2) molten spray, (3) shrapnel, and (4) large, slow moving fragments of the target assembly. However, no imaging data exists. The second purpose of this LDRD is to design an optical imaging diagnostic suitable for measuring the properties of the post-shot debris environment on Z.

This report, and the work herein, was jointly funded funded via a Strategic Partnership with Keith Matzen and the Assured Survivability and Agility with Pulsed Power (ASAP) Mission Campaign. It is separated into two sections: Optical imaging of (1) fast phenomenon using modified optics of the Z Line VISAR system and (2) the post-shot debris environment on Z. The fast optical imager, called SEGOI (Self-Emission Gated Optical Imager), was fielded on four different experimental campaigns, enabling measurements of power flow plasma expansion from transmission line surfaces, the post-post plasma generation in a dynamic screw pinch target, the implosion dynamics of a seeded magneto Rayleigh-Taylor Z pinch target, and the emission from a Magnetized Liner Inertial Fusion (MagLIF) target.

In the second section, we present imaging data of the post-shot debris environment, which persists for tens of milliseconds after the Z shot. Collaborating with the Sandia Photometrics Group (1535), debris particles were tracked in order to enable later-time velocity measurements of the debris field.

2. OPTICAL IMAGING OF FAST PHENOMENON ON Z

2.1. Introduction

Optical phenomenon on Z (i.e. emitting in visible wavelengths) are ubiquitous. They can arise from the enormous electrical current densities that produce plasmas on transmission line surfaces and in anode-cathode (AK) gaps. These so-called "power flow" plasmas are hypothesized to have dramatic effects on Z. First, current shunting across these plasmas is one possible mechanism for multi megaAmpere current losses in the transmission line leading up to Z targets. Second, these plasmas may actually modify the implosion dynamics of Z targets themselves. In one example, simulations predict low density plasmas in MagLIF flux compress the applied axial magnetic field on the surface of the liner to large values, changing the morphology of the magneto Rayleigh-Taylor (MRT) instability from azimuthally symmetric to helically oriented. These plasmas may also re-distribute current near the targets themselves, providing larger radii and lower inductance parallel current paths to Z targets. For ICF targets such as MagLIF, current re-distribution could reduce the available magnetic drive pressure at stagnation, ultimately impacting the target performance.

The current state of the art for optical emission measurements on Z is fiber-based. This includes the streaked visible spectroscopy (SVS) system, which is useful for measuring the plasma temperature, density and magnetic field, and chordal photonic-doppler velocimetry[2] which enables line-integrated density measurements. However, a key limitation to both of these diagnostics is they are limited to single line-of-sights (LOS) with limited spatial resolution ($\sim$100-200 μm). This makes it difficult to interpret the spatial dynamics of the system, as "images" must be assembled from discrete fibers, therefore limiting spatial resolution and field of view (FOV).

Addressing this, our LDRD developed the first optical imaging diagnostic for recording side-on emission of Z targets and transmission lines since Z's refurbishment. The diagnostic leveraged the Z Line VISAR (ZLV) infrastructure.[3] In the follow sections, we discuss the development effort for this diagnostic followed by an overview the first measurements of the system, which was fielded on four separate campaigns from the Power Flow and Inertial Confinement Fusion (ICF) programs.

2.2. Diagnostic Design

The diagnostic developed for this LDRD is called SEGOI (Self-Emission Gated Optical Imager). SEGOI leverages the existing ZLV infrastructure, which provides top-down VISAR and self-emission measurements of the top of Z targets. ZLV is a world class system that

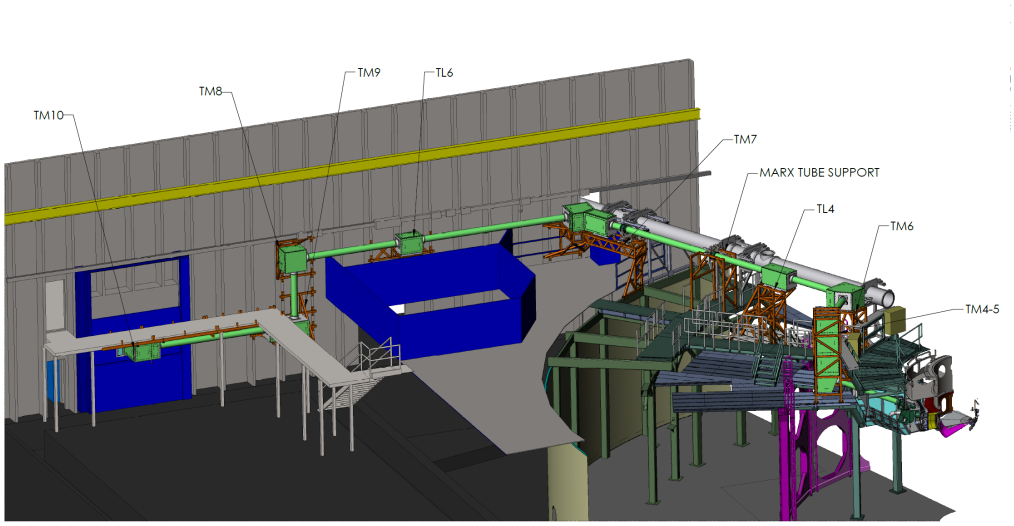

Figure 2-1. Z Line VISAR optical relay beam path in 983.

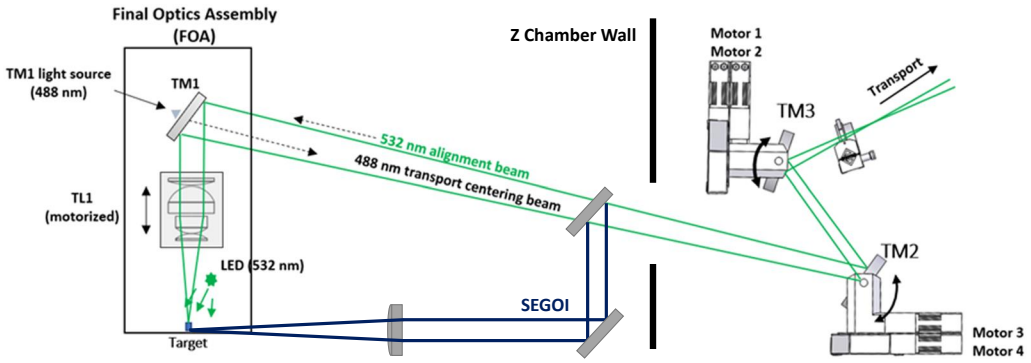

Figure 2-2. Top-down and Side-on implementations of the Z-Line VISAR system.

relays visible light from the Z center section to two streak cameras and eight gated optical imagers to an annex room outside the high bay. The beam transport system, shown in Fig. 2-1, is 50 m long and relays 540-600 nm light to the GOIs and 532 nm light to the streak cameras. The streak cameras record up to 64 and 92 ns, while the GOIs have gate widths of 100 ps to 10 μs and are limited to a maximum interframe time of approximately 50 ns. The system was primarily designed for line VISAR; as such, the resolution on the streaked cameras is excellent ($\sim$10 μm). The GOIs have significantly worse resolution ($\sim$50 μm) as they were a secondary addition the ZLV system designed to look at large scale features.

Designing a suitable side-on system for routine diagnostic deployment was non-trivial. First, the expense of consumables must be significantly reduced (ZLV is $\sim$\$50k in consumables, which is not practical to implement when the primary objective is not related to the

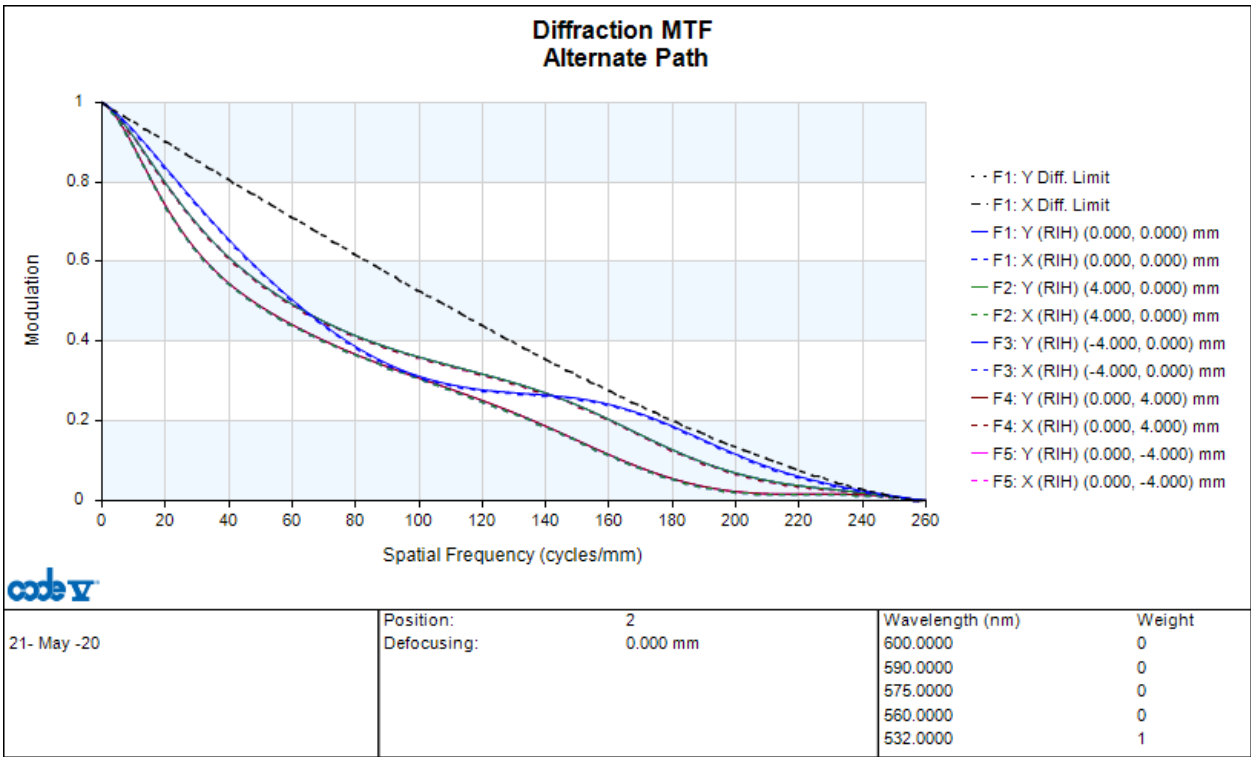

Figure 2-3. MTF for SEGOI calculated using Code V.

diagnostic). Second, the optical beam path is different and must vary from shot-to-shot to accommodate different target heights. Third, the diagnostic must offer quick installation (∼30 min.) to prevent undue delays to the Z shot timeline. Some of these requirements are not as stringent compared to the ZLV system: ZLV is a front-back system (where the probe and collected laser light are transported through much of the same optics) and the f-number (F/2) is designed to collect light reflected off shock fronts that deflect rays to very wide angles.

Teaming with Org. 6783, we designed an optical system by modifying the Code V ray trace of the original ZLV system (see Fig. 2-2). To meet the first requirement, we identified a COTS lens from Edumnd Optics (75mm Dia. x 400 mm focal length, MgF_2 Coated, Achromatic Doublet Lens) for $250. When placed ∼450 mm from the target, Code V calculations showed this would yield a FOV of ∼8-10 mm with a resolution of ∼30-50 μm. The Modulation Transfer Function (MTF) is shown in Fig. 2-3.

With a lens identified, we designed a consumable COTS periscope and lens mounting system. The periscope consists of two mirrors that direct the optical axis to view Z targets side-on. The mirrors are fixed with RTV silicone to smooth-bore kinematic mirror mounts with two adjusters. The mirror mounts are connected to a vertical rail to allow for the additional adjustability required to accommodate a variety of target heights (meeting the second requirement above). The lens is mounted to a rail-slider to allow forward-backward adjustment for focusing. The system is pre-aligned on an optics table in 983 Phase B (Mykonos)

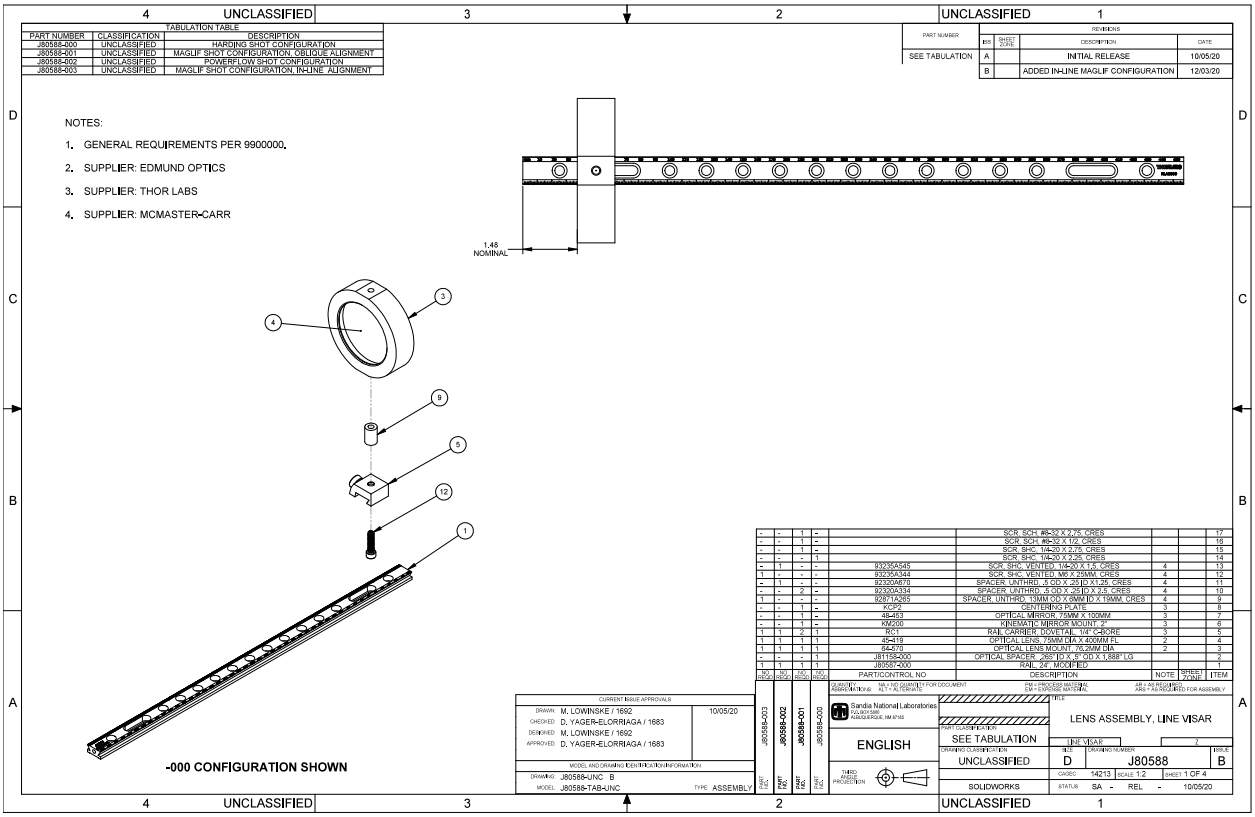

Figure 2-4. SEGOI lens assembly

using a <5 mW eye-safe alignment laser. The total cost for the lens and periscope assemblies is ∼$2k. A consumable 6 inch diameter blast-shield window (∼$1k) is also required to prevent debris from penetrating the vacuum window. Overall, the consumable cost is roughly $1/20th$ the cost compared to ZLV. The lens and periscope assemblies are shown in Figs. 2-4-2-7.

As mentioned above, the third requirement is that the system must offer quick installation in the Z center section. As the periscope and lens assemblies are light-weight (<5 lbs), they do not require the Z crane system for installation and can be hand-passed to center section personnel. The rails bolt directly to the MITL deck plate. This process takes less than 5 minutes.

Alignment is performed using the ZLV alignment laser. Prior to installation in the chamber, alignment targets are printed on white paper and fixed to the mirrors and lenses. The ZLV alignment laser is first aligned to the center of the top mirror. The alignment target is then removed and the beam is aligned to the center of the bottom mirror using the

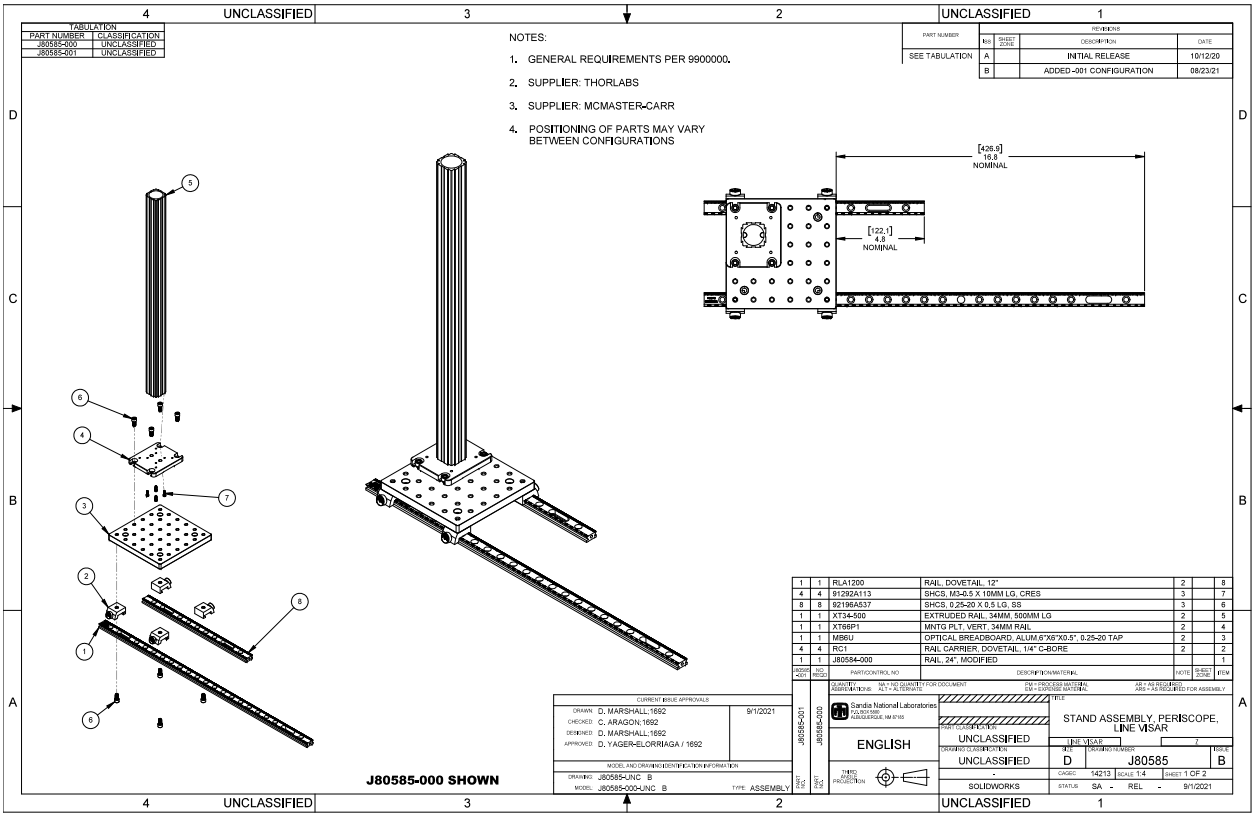

Figure 2-5. SEGOI periscope base plate assembly.

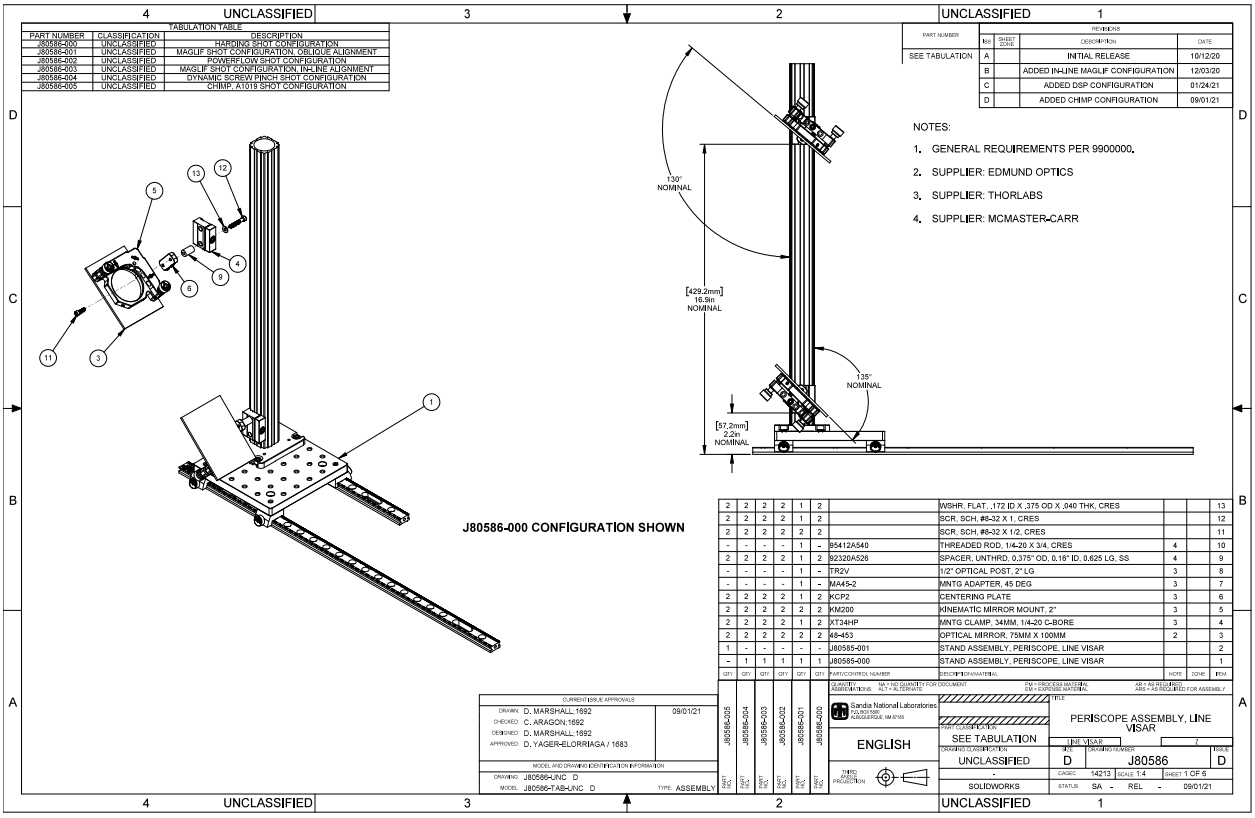

Figure 2-6. SEGOI complete periscope assembly.

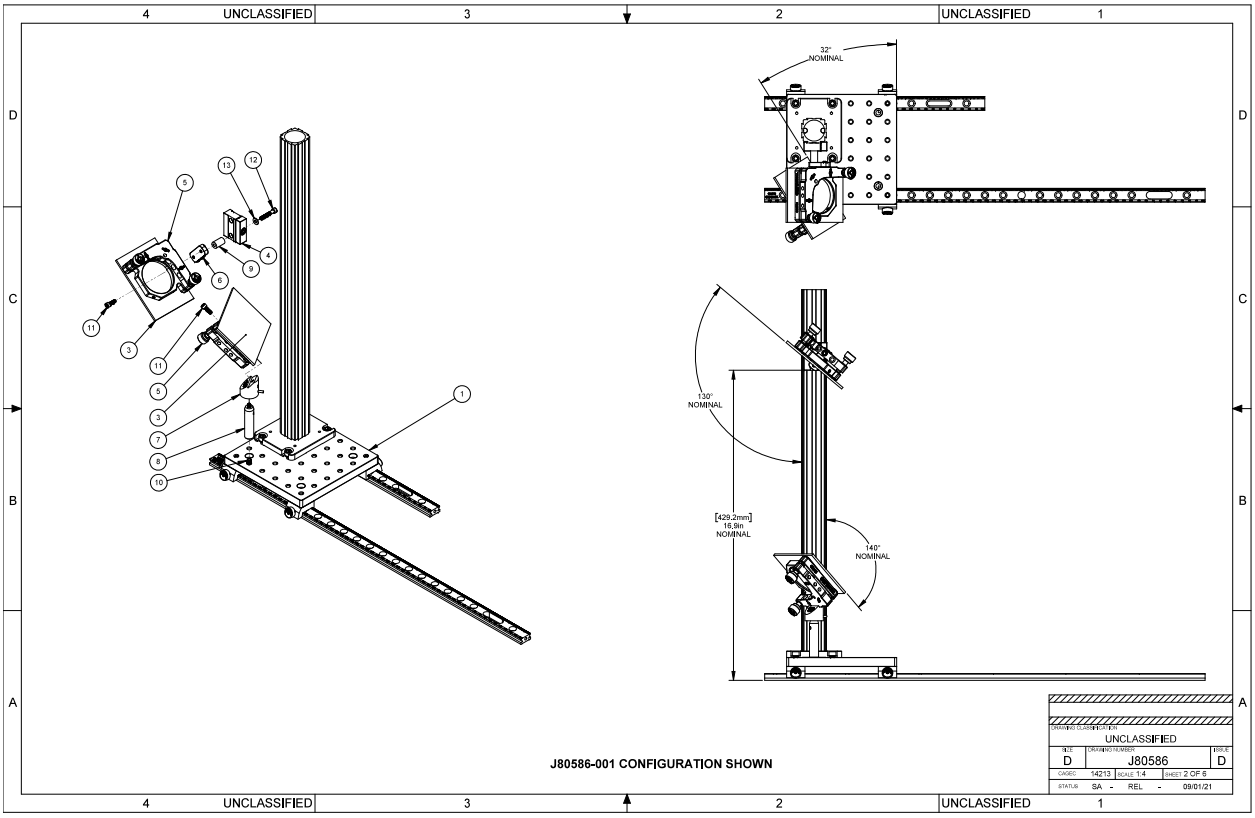

Figure 2-7. SEGOI periscope assembly with wide-angle mirror-mount option. The bottom mirror assembly is connected directly to the base-plate and allows wide angles (exceeding 3 deg. mirror mount limit) for configurations that seek to probe the target at non-standard angles (i.e. not directly from LOS 110).

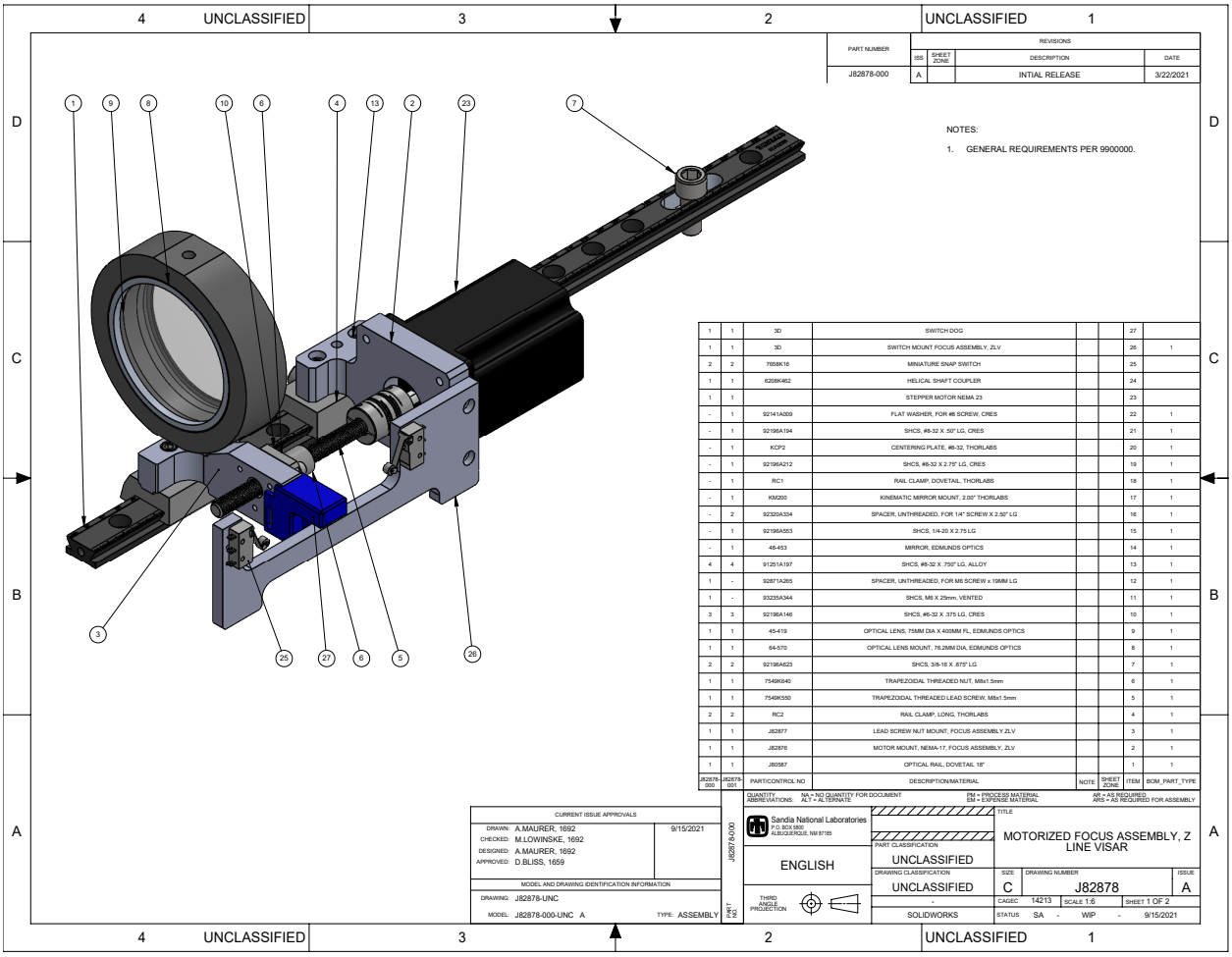

Figure 2-8. Lens assembly with remote control. The miniature snap switch prevents over-driving the lens beyond the rail.

adjusters on the top mirror. The alignment target on the bottom mirror is then removed and the beam is aligned to the center of the lens (the alignment target is then removed from the lens). The lens focuses the alignment beam from a ∼3 inch diameter to a small point (∼1 mm). Using the bottom periscope mirror adjusters, this point is directed to the target or region of interest.

Once the alignment laser is pointed at the target, in-chamber LEDs mounted to the aperture ring in the load hardware and controlled by the ZLV software are powered on. These LEDs can be configured to back-, side-, and/or front-light the target. The ZLV alignment camera collects an image, which is focused by adjusting the lens position forward and backwards. The bottom periscope mirror then adjusts the location of the field of view of the target. This last step is not ideal as the optical axis is no longer centered on the lens, but is presently required to quickly align and focus the system. In total, installation and alignment is completed in approximately 30 minutes.

To improve the installation timeline, we designed a remotely controlled lens focusing

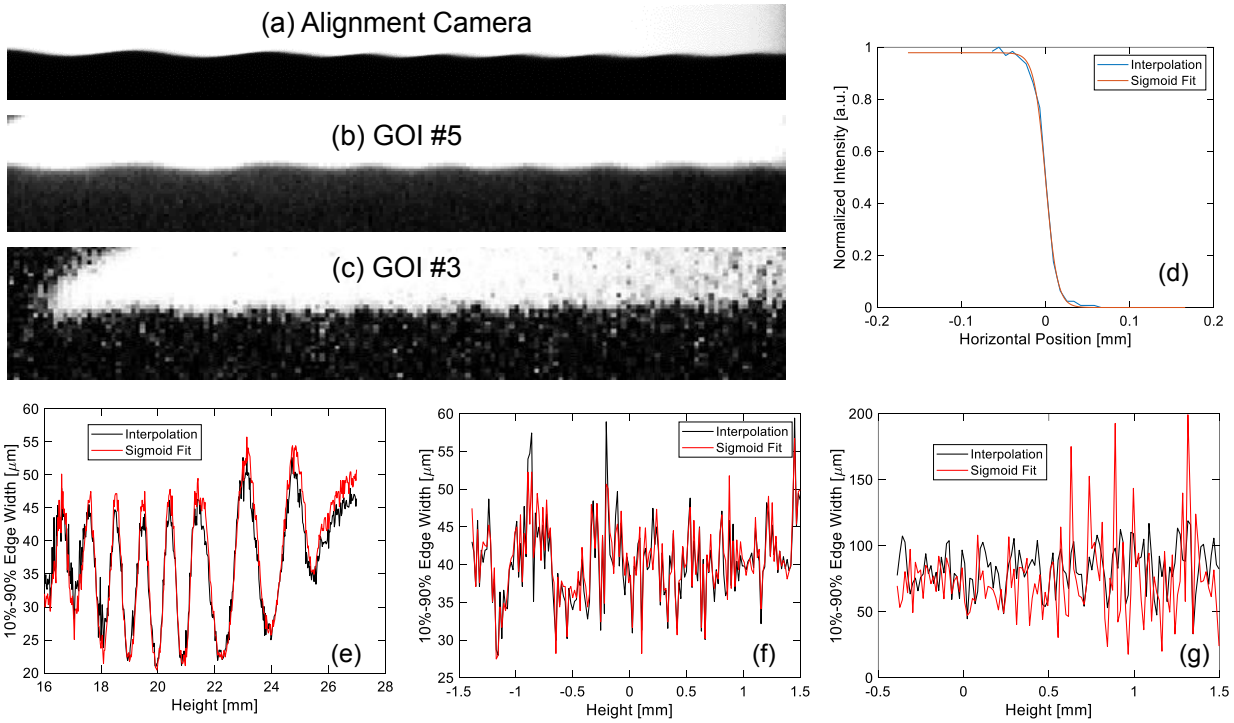

Figure 2-9. (a)-(c) Backlit images of an aluminum liner seeded with sinusoidal perturbations. (d) Interpolated and sigmoid-fit intensity profiles used to determine the edge width. (e)-(g) Edge widths for the different cameras in (a)-(c) plotted as a function of height. The minimum edge widths correspond to regions in the images that are unblurred by the 3D nature of the target.

system, shown in Fig. 2-8. This system is controlled by the ZLV infrastructure and allows forward-backward motion of the lens along the rail. 3D printed parts fix the motor to the rails. During installation, the motor-lens assembly is manually adjusted until a reasonable image is obtained. The rail-slider corresponding to the motor is then locked in place. The focus can then be improved by driving the motor and thus pushing the lens forwards or backwards. This can be performed concurrently with other chamber activities (e.g. additional diagnostic alignment, vacuum pumpdown, etc.) and will be tested on a future experiment.

Due to the strict Z timeline, we have not had an opportunity to field a resolution target. Therefore, we must assess the performance of the system based on pre-shot target images. In Fig. 2-9(a)-(c), we show images of the edge of an aluminum liner that has been seeded with 600 μm and 338 μm wavelength modes. The amplitude of the modes is 2.5% of the wavelength. The alignment camera offers the best quality image overall, indicating the overall optical system is well-designed. Unfortunately due to the GOI configuration (specifically, the optical beam-splitting in the ZLV annex) the quality is degraded. The cleanest image was obtained on GOI-5, with GOI-3 being one of the worst.

To quantify the resolution, we use the 10-90% edge width. The edge consists of <10 pixels, which necessitates interpolation or fitting of the intensity. To accomplish this, we

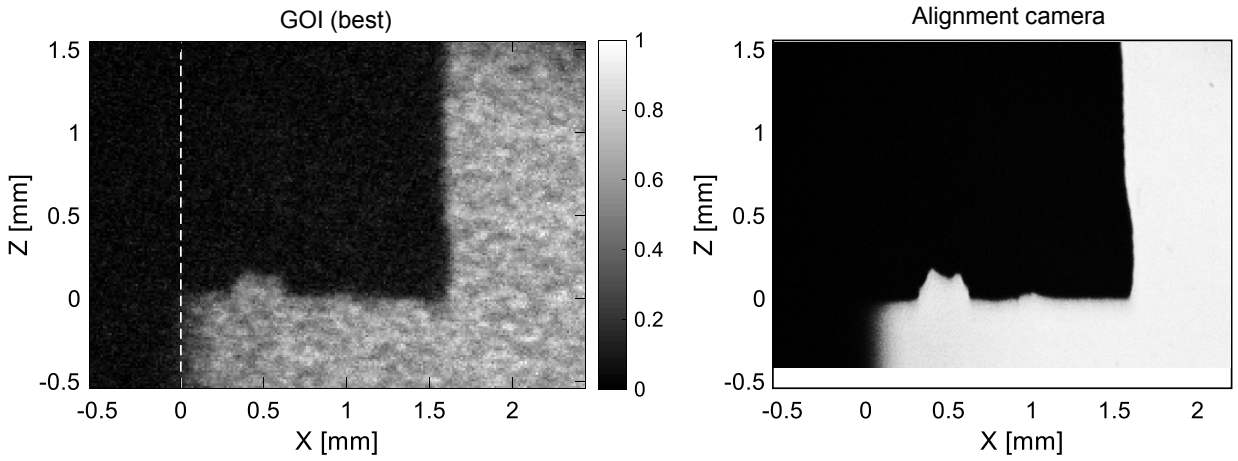

Figure 2-10. Comparison of alignment camera and GOI images of a 3D printed resolution target.

first normalize the intensity in the edge region. Backlight (bright) regions are normalized to unity while the regions obscured by the liner are normalized to zero. The pixel intensity is interpolated to a fine grid (typically 1000 points) or fit using a sigmoid function, as shown in Fig. 2-9(d). In Figures 2-9(e)-(g), the edge width is plotted as a function of height for the alignment camera and two GOI images. Examining the alignment camera image, we see that part of the sinusoidal ripples between the spikes and bubbles are blurry. The effect is due to a small angle between the optical axis and the axis orthogonal to the target's Z axis. This allows the back parts of the azimuthally symmetric target to be imaged. Since they are out of the plane of focus, they blur the edge slightly. Therefore, to quantify the edge widths we take the regions where we expect sharp edges (e.g. the peaks of the perturbation). This yields edge widths of $\sim$20, 30, and 50 μm for the alignment camera, GOI-5, and GOI-3, respectively. Therefore, we expect that with improvements to the GOI cameras and configuration the system could have a resolution of $\sim$20 microns.

Another example comparing the image quality on the best GOI to the alignment camera is shown in Fig. 2-10. For these images, we 3D printed a resolution target using a 25 μm layer height. Unfortunately, the quality of the print was insufficient to enable a measurement the resolution (the very fine "teeth" were not able to be printed); however, qualitative comparison of the image from the alignment camera and the GOI shows the stark quality difference between the two cameras.

While the intent of this LDRD was to demonstrate that self-emission imaging is possible on Z, future upgrades could significantly improve the system. A dedicated housing could be designed for the periscope and lens systems, which could be remotely controlled. Furthermore, additional mirrors after the lens could direct the optical axis to the target and eliminate the beam steering through the lens. The lens itself could have tip/tilt and angular rotation to better improve the quality of the images. If the lens is sufficiently protected so that it is no longer consumable, a larger diameter lens could be implemented to improve resolution.

2.3. Power Flow

SEGOI was commissioned on the Power Flow Diagnostics 20a shot z3558 on November 30th, 2020. Total installation and alignment time was approximately 1 hour (this has been reduced to 30 minutes as the system is exercised more frequently). A rendering of SEGOI and the power flow load hardware is shown in Fig. 2-11. The optical axis is initially along LOS110 and directed toward the z-axis of the target. For this experiment, a small 1x1 in. mirror (indicated in green in Fig. 2-11(b)) re-directs the axis to point between the anode-cathode (AK) gap formed between the 6 cm radius cylindrical cathode and anode post (note the 6 slots and posts in the image). The view of the target region from the mirror is shown in Fig. 2-11(c) (note the resolution target, which attaches to the mirror, is included in the rendering but was not fielded on the shot). On the right of the image is the 6 cm radius cathode. On the left is the anode post, with the angled edge of the post directed towards the AK gap. The dashed line indicates the orientation of the streak camera slit.

The data acquired from the streak camera is shown in Fig. 2-12. The images on the left and right are of the same data but with differing data scale limits to highlight dim and bright features. Examining Fig. 2-12(a), we see early time oscillations in intensity on the cathode edge. It is important to note that these oscillations may be due to (1) oscillations of intensity at a fixed position and/or (2) axially propagating waves that appear as oscillations from a 1D perspective. These oscillations are highlighted in Fig. 2-13(a), with a vertical lineout in (b) and Fourier spectrum analysis in (c). The frequency of the oscillations appears to increase until they cease at 3025 ns. Based on the Fourier analysis, the dominant periods are between 1.8 and 2.5 ns (a time-dependent FFT could better elucidate the time-frequency behavior). At 3025 ns, the cathode emission begins to significantly increase, and plasma appears in the AK gap on both the anode and cathode edges. As previously discussed, this 1D diagnostic cannot differentiate between plasma propagating axially or radially; however, the plasma that extends across the gap decays in brightness around 3060 ns. Around this point, plasma appears to expand from the cathode surface towards the anode. Two-dimensional images from the GOIs (discussed later) show this plasma does indeed expand from the cathode and is not due to axially propagating plasma.

Interestingly, the emission on the cathode itself shows temporal dynamics, as shown in Fig. 2-12(b). A lineout of the cathode at $R = 4.8$ mm, along with a plot of the average intensity of the cathode region, is shown in Fig. 2-14. Here, we see that the rate of the cathode emission as a function of time significantly decreases at 3030 ns (this may be a good metric for when the cathode fully breaks-down). Afterwards, there are weak oscillations in intensity on the cathode surface. Fourier analysis shows these have a period of 5.9 ns.

The first shot did not acquire usable GOI data. Contrary to what we expected, the cameras were fully saturated. On the second shot, z3569, we reduced the gates and gains on the cameras and acquired two usable frames of data at 3096 ns and 3102 ns, shown in Fig. 2-15. Earlier frames were too dim with no usable data (not shown). Based on the pre-shot image, we identify the edge of the anode post (left side) and edge of the cathode (right side). While difficult to see in the image, the cathode edge has a relatively bright line on its surface from LED light. These boundaries are shown on the GOI images on the

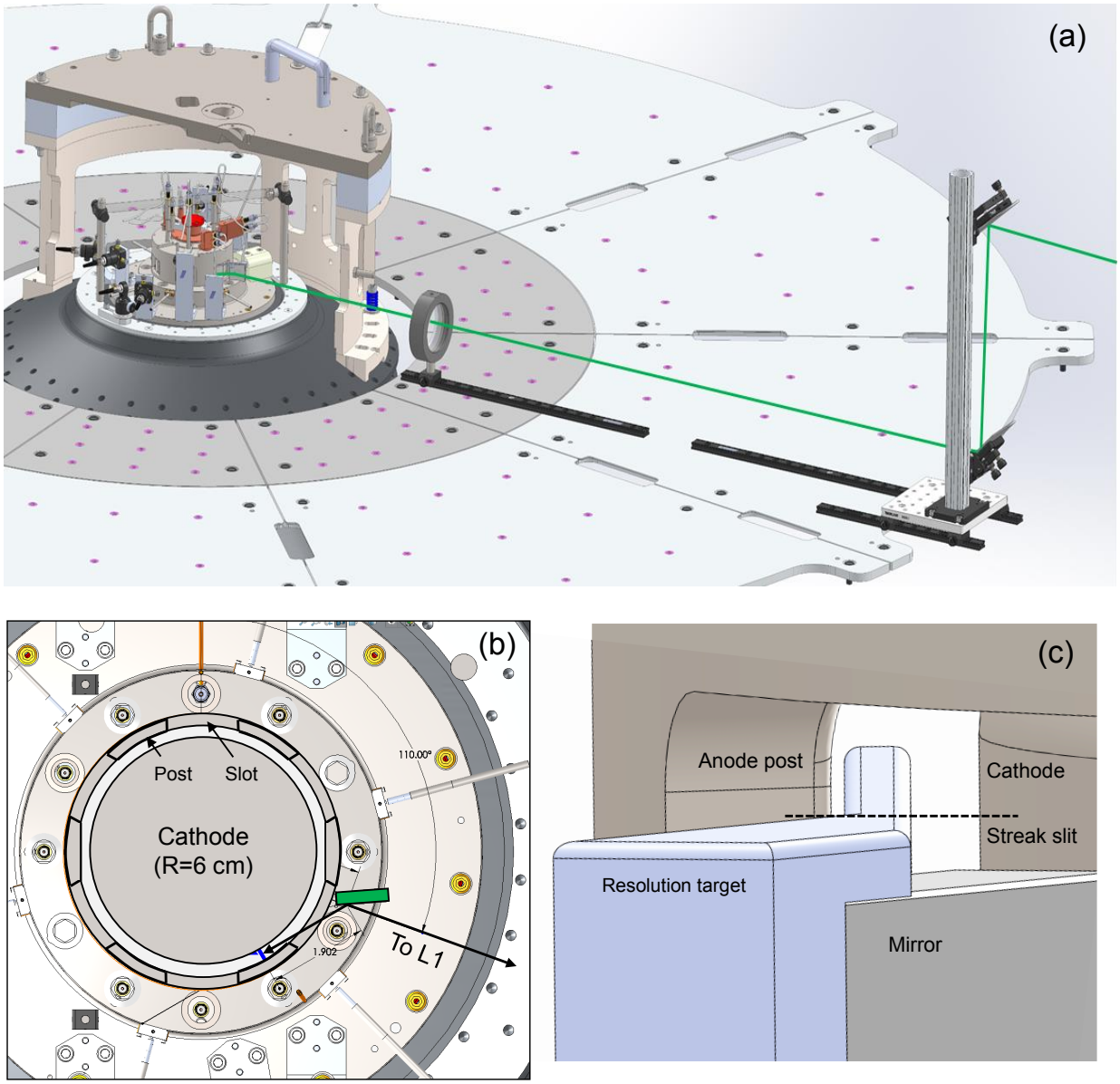

Figure 2-11. (a) Diagnostic and load hardware configuration for the Power Flow Diagnostics 20a campaign. (b) Top-down cross section of the hardware, indicating the location of slots and posts on the anode return can, the mirror (green), the target area (blue), and the optical axis (black lines). (c) Approximate view of the diagnostic. Note the resolution target was removed for the experiment.

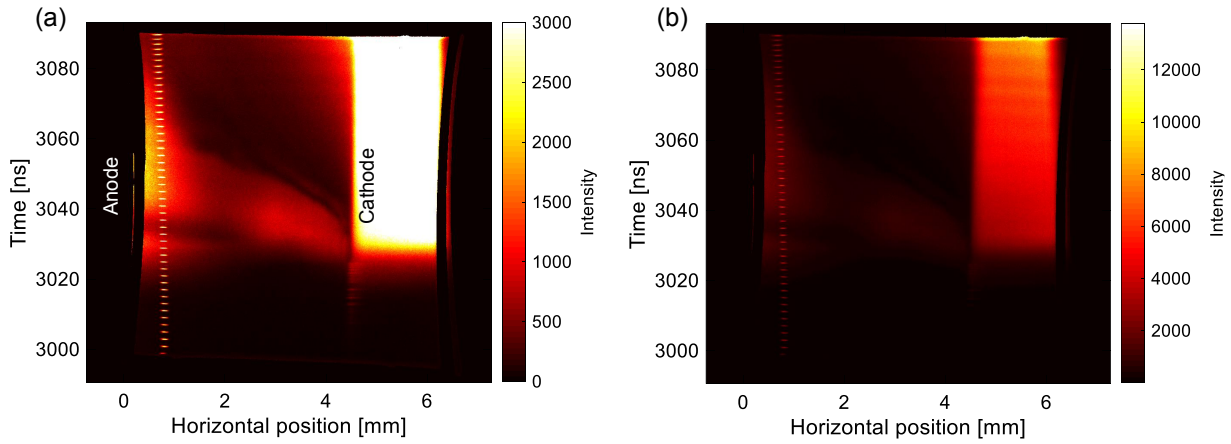

Figure 2-12. SEGOI streak data from z3558. The two images are of the same data but with different data limits to highlight low and high intensity features.

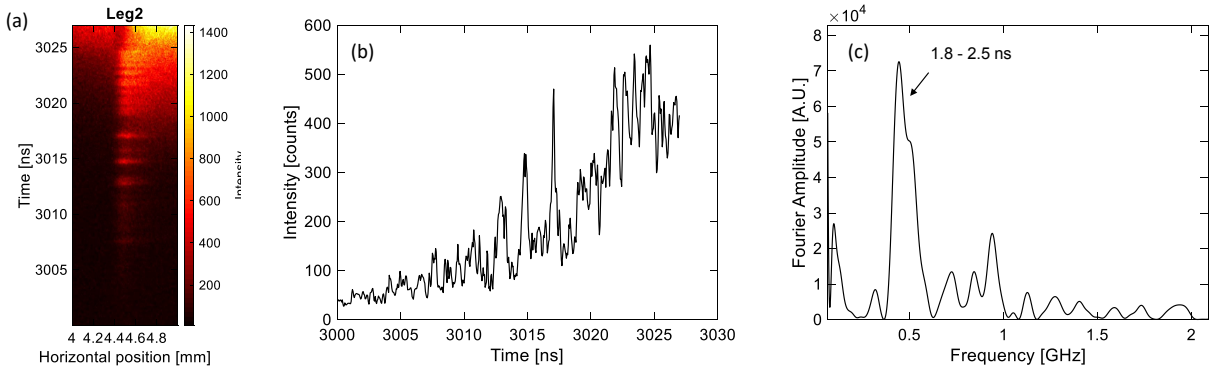

Figure 2-13. (a) Streak image of early-time oscillations on cathode surface. (b) Intensity lineout on cathode surface. (c) Fourier analysis of emission oscillations, showing a period of 1.8 to 2.5 ns.

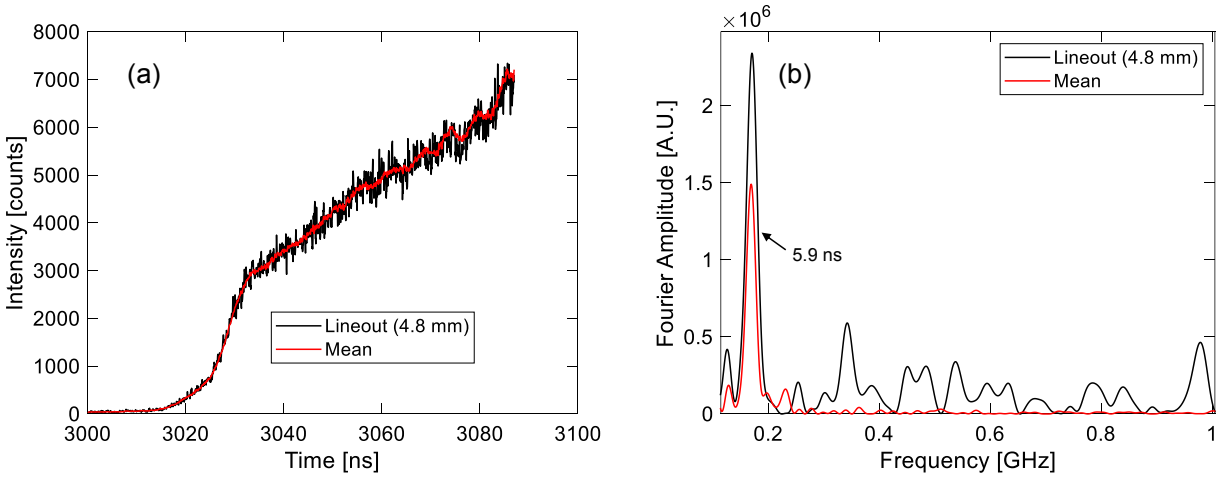

Figure 2-14. (a) Intensity lineout through cathode and mean cathode emission showing full breakdown at 3030 ns. (b) Fourier analysis of emission oscillations, showing a dominant period of 5.9 ns.

right. Interestingly, there is about 1 mm of plasma that has formed on the anode that grows in intensity between frames. The cathode shows even more complex dynamics. Plasma has expanded over 2 mm into the gap and is non-uniform in its axial extent. Plasma is also seen to expand between the two frames, conspiring to close the gap and possibly redistribute current from the Z target down-stream.

While the origin of these dynamics is not presently understood, we see that SEGOI has offered a valuable insight into the plasmas produced from current carrying surfaces on the Z Machine. This diagnostic will continue to be fielded on future Power Flow campaigns.

2.4. Dynamic Screw Pinch

SEGOI was fielded on on the Dynamic Screw Pinch (DSP) ICF experiments, z3577 and z3585. The DSP is a novel concept that utilizes helically oriented return posts to generate a helical magnetic drive field on the surface of the liner that rotates toward the horizon as the target implodes.[4; 5; 6] By dynamically rotating, the magnetic field consistently applies a stabilizing magnetic tension that is designed to reduce the overall growth of the magneto Rayleigh-Taylor (MRT) instability. A critical requirement of the platform is that current must flow helically through the return posts. Any post-to-post shorting due to plasmas that form between the posts can redistribute the helical current axially and thus limit the efficacy of the stabilizing mechanism. Complete post shorting could, in an extreme example, cause the liner to implode with a purely azimuthal magnetic field and thus develop m=0 sausage MRT modes that freely grow with no magnetic tension.

In Fig. 2-16, we show GOI images acquired during shot z3577 (due to a timing issue, no usable data was acquired for z3585). The diagnostic view is shown in the top-left, marked with a red circle. This shows the overall target, including the helical posts in front of

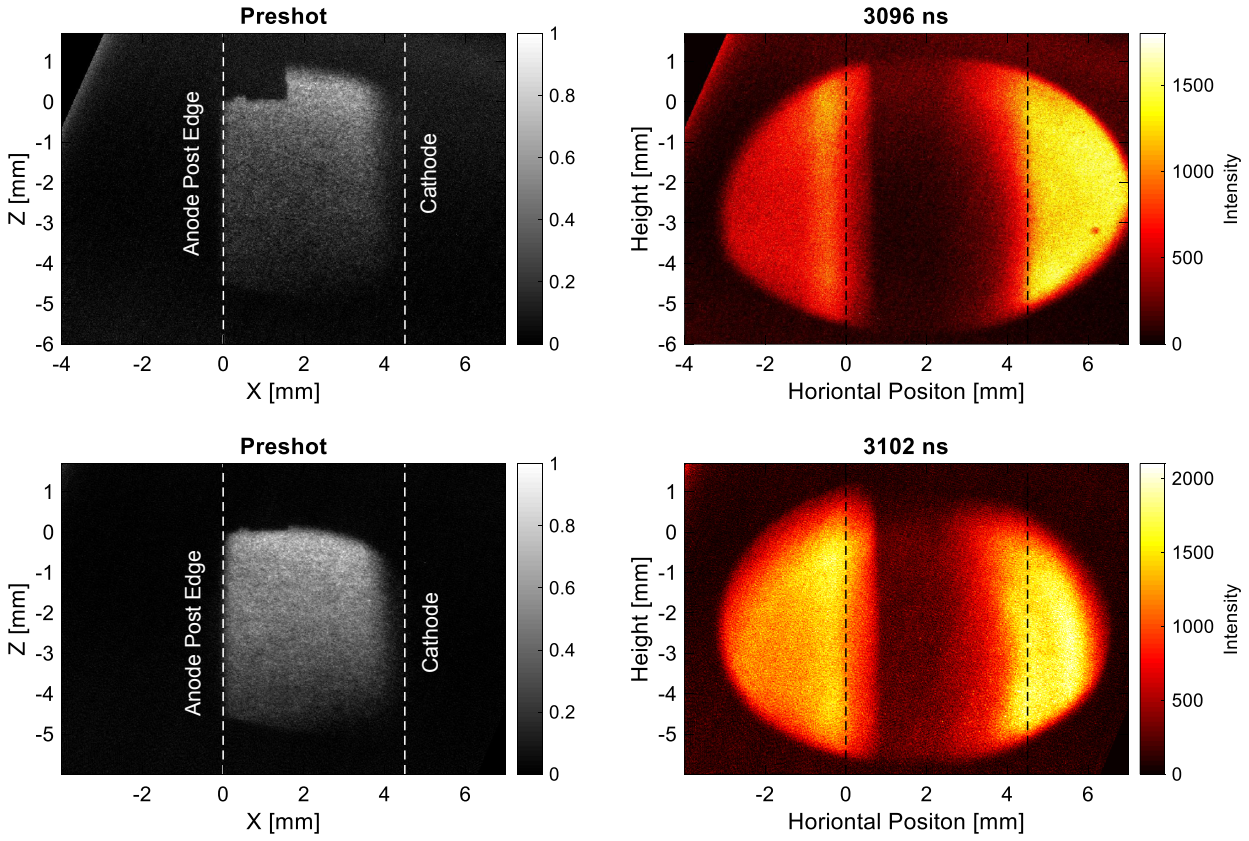

Figure 2-15. Preshot and GOI data at 3096 and 3102 ns, showing non-uniform plasma expansion into the AK gap.

the liner. The initial radius of the liner is indicated in the dashed vertical lines. For these experiments, the GOIs were configured with a gain setting of 200 and gate of 200 ps. As seen in the figure, the liner emission was extremely bright and saturated the cameras. As time continues (particularly by 3075 ns), it is clear the liner has begun to implode. The sequence of images also show optical emission from the posts. Plasma from the post edges appears darker than plasma from the liner, indicating this plasma is at least partially opaque to the visible light from the liner. The post plasma expands significantly, developing instabilities in the process. Around 3063 ns, plasma from the central and bottom posts have started to connect. By 3075 ns, this plasma almost completely obscures emission from the liner. Unfortunately, the last two frames are almost fully saturated.

This post-to-post plasma may be responsible for shorting helical current and, as previously mentioned, reducing the efficacy of the DSP mechanism. Interestingly, the experimental radiography indicated a predominantly $m = 0$ structure, which is consistent with a strong azimuthal component of the drive field (compared to the solenoidal axial component from the helical posts). Future DSP designs will attempt to limit this post-to-post shorting by increasing the axial spacing between the posts and relaxing the helical pitch angle of the posts to limit electric field stresses.

High quality streak data was acquired for both z3577 and z3585, shown in Fig. 2-17. The images are complicated by the post in the center of the FOV, which expands and occludes the liner emission. For z3585, we adjusted the axial location of the streak slit so that the post was offset to the right, allowing the liner edge to be tracked later in time. Both images show plasma emission on the liner around 3025 ns. Interestingly, this plasma shows strong azimuthal correlation, something not predicted by the linear theory or 3D simulations of DSP targets. Helical perturbations would show as bright dots as a function of radius. Around 3050 ns, there is a $\sim$10 ns burst of emission on the liner surface, whose origin is entirely unknown. Note the bright horizontal bands in the image are due to the Z Beamlet-Laser (ZBL), which is used to drive the x-ray source for radiography. ZBL generates a pre-pulse before the main pulse. All four pulses are captured by the diagnostic and serve as timing fiducials.

The edge of the liner can be tracked to determine the implosion trajectory. This was done for z3577 by first normalizing the image to the emission of the liner (towards the center, away from the edge). Then, the 30% and 50% emission thresholds were tracked radially inward, and are plotted in Fig. 2-17(c). For z3585, the liner boundary was manually tracked. Shot-to-shot variations are small and overall the implosion trajectories follow a similar path. This data will be compared to radiography data.

2.5. Magneto Rayleigh-Taylor Experiment

A single experiment was conducted to investigate the scaling of the magneto Rayleigh-Taylor instability as a function of peak current, with the hypothesis stating that MRT growth obeys self-similar scaling laws. This experimental campaign is an important part of the ICF scaling argument, where campaigns including MagLIF depend on conserving instabilities as

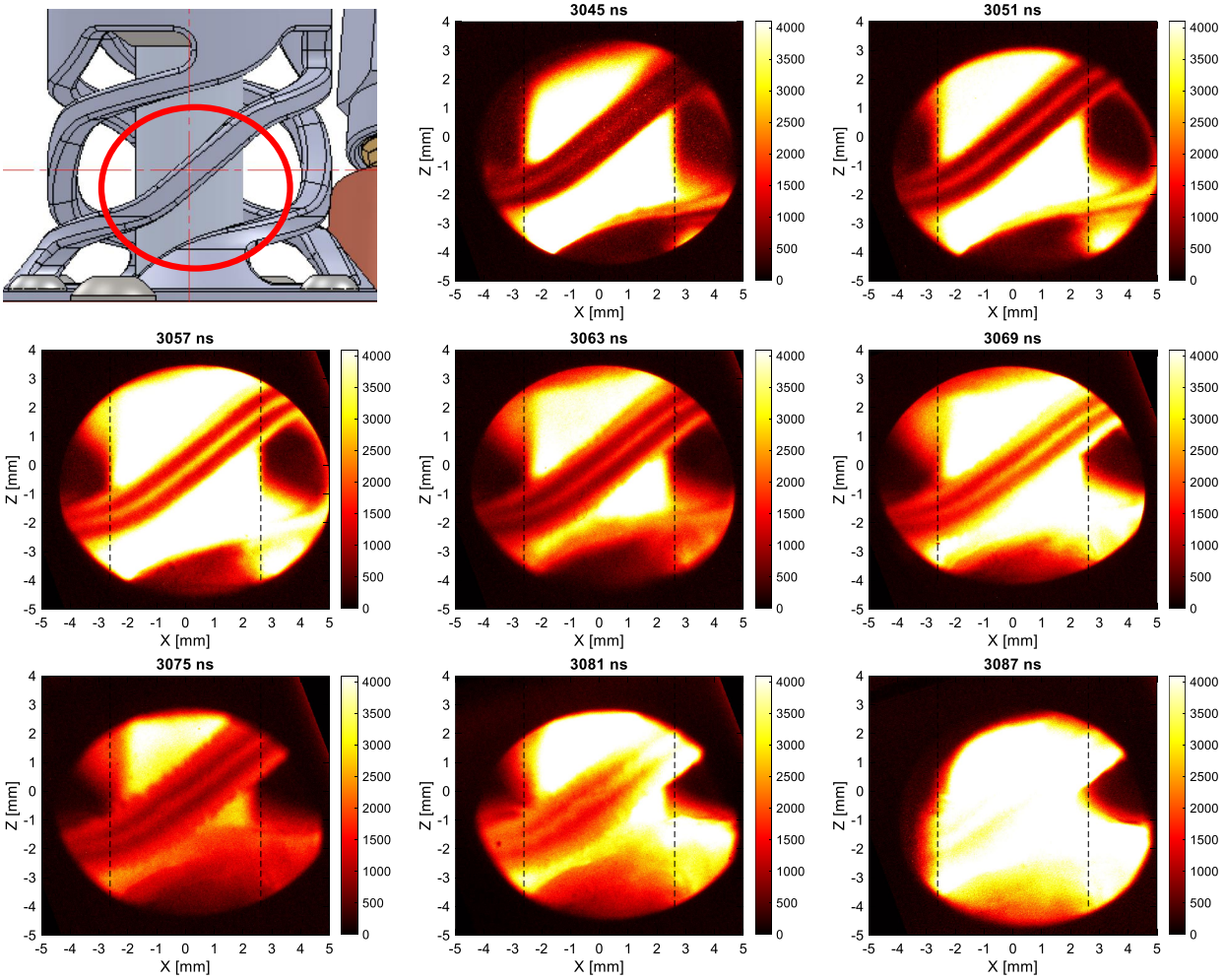

Figure 2-16. SEGOI field of view (red circle) and self-emission data. The vertical dashed lines indicate the initial position of the liner.

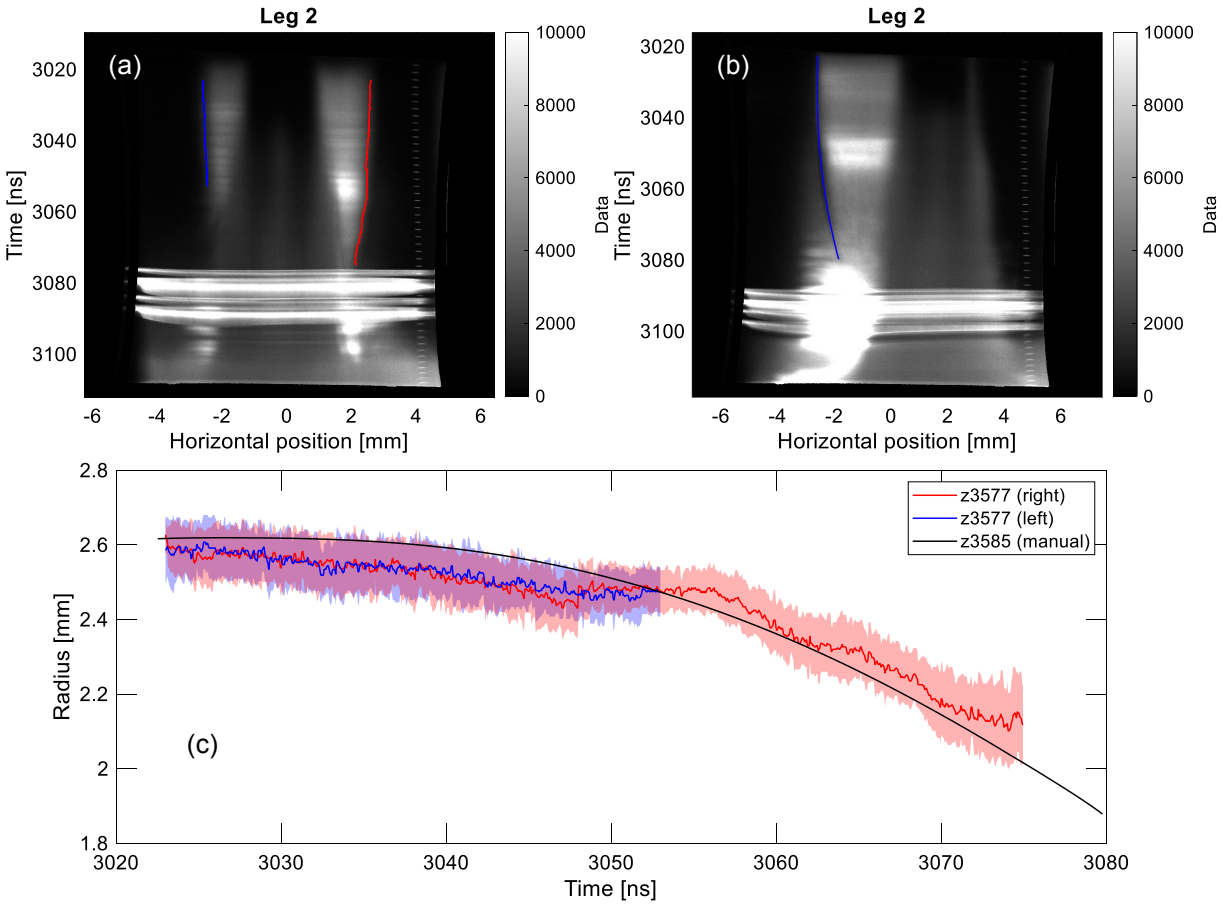

Figure 2-17. Streak data for z3577 (a) and z3585 (b). The return post is in the center (right) part of the image for z3577 (z3585) and continuously expands throughout the current pulse. The bright horizontal lines are due to the ZBL backlighter source. (c) The liner outer radius for both shots, identified using a tracking algorithm (z3577) that tracks 30% and 50% emission thresholds and manually (z3585). The emission thresholds give the differences in radius, with the mean value indicated in red and blue.

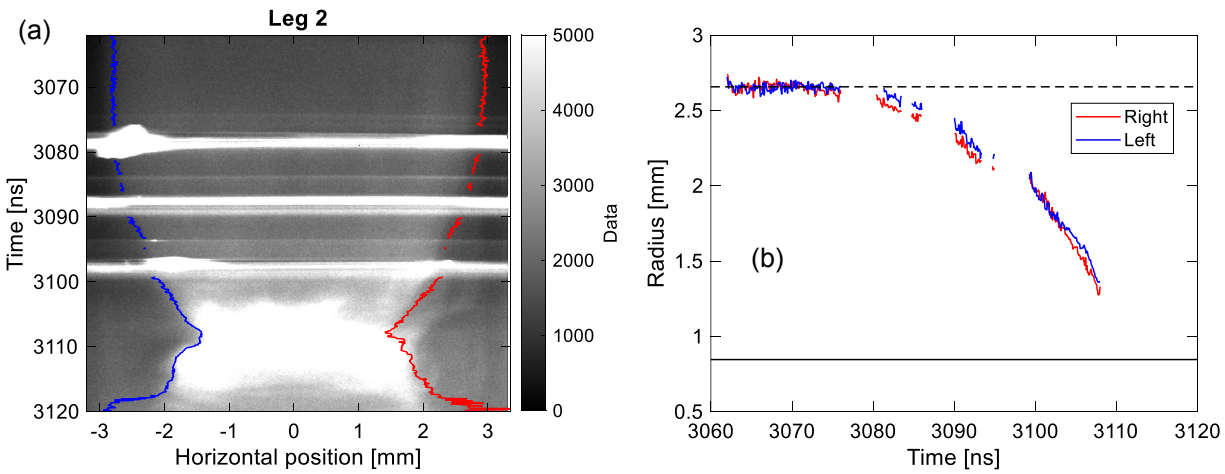

Figure 2-18. Streak data for z3614. The MRT bubble trajectory for the 600 μm wavelength mode is tracked and plotted in (b). The bright horizontal bands are due to a single pulse from Z-Petawatt and two pulses from ZBL for radiography. The initial radius of the bubbles is indicated in the black dashed line, and the radius of the on-axis tungsten rod (for limiting x-ray self-emission) is indicated by the solid black line.

current is scaled to next generation pulsed power machine levels. The experiment, z3614, was a Lincoln seeded-MRT target, consisting of an aluminum liner seeded with sinusoidal perturbations. The target was scaled down to 14 MA based on a 19 MA version that was originally fielded in 2010.[7; 8] Two wavelengths were fielded, including 600 and 338 μm, with the former included to test the scaling of growth with wavelength and the latter included to test the scaling of growth with peak current by comparing to the 19 MA version.

For z3614, the streak camera was configured to image a bubble (valley) region of the 600 μm perturbation. These were predicted to implode significantly more than the spike (peak) regions. Figure 2-18 shows the streaked image acquired from this target. The spacial scale was normalized so that the emission boundary before 3070 ns was set to the initial liner position. The emission boundary was tracked by normalizing the image to the intensity at $R = 0$ mm and then tracking the 50% boundary radially inward. These trajectories are plotted in Fig. 2-18(b), and show overall good agreement between the left and right sides of the liner. Around 3110, the self-emission significantly increases as the liner nears stagnation on the on-axis tungsten rod ($R = 0.87$ mm). This data will be valuable to compare to radiography (2 frames acquired per experiment) and simulations.

The GOI images were extremely faint as we expected significant emission from the aluminum liner and configured the gain and gate settings accordingly. One usable (albeit noisy) frame was acquired at 3079 ns, shown in Fig. 2-19. Unfortunately, the boundary and instability amplitudes are not trackable; however, local mean smoothing reveals bright and dark regions in emission. In Fig. 2-20, we compare the horizontally averaged emission of the smoothed and un-smoothed data to the interface position measured from the pre-shot. Here, we see a very strong anti-correlation, with bubble regions emitting more light than the spike

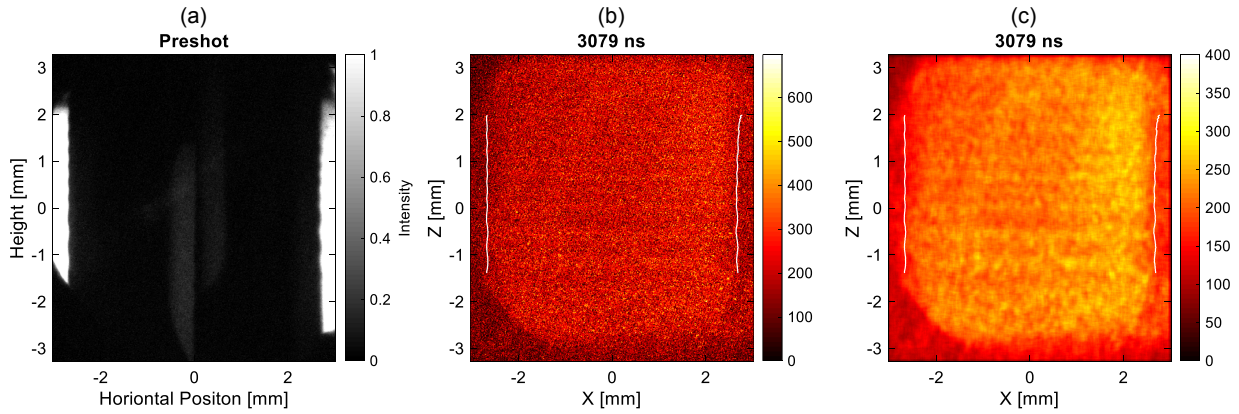

Figure 2-19. MRT GOI data

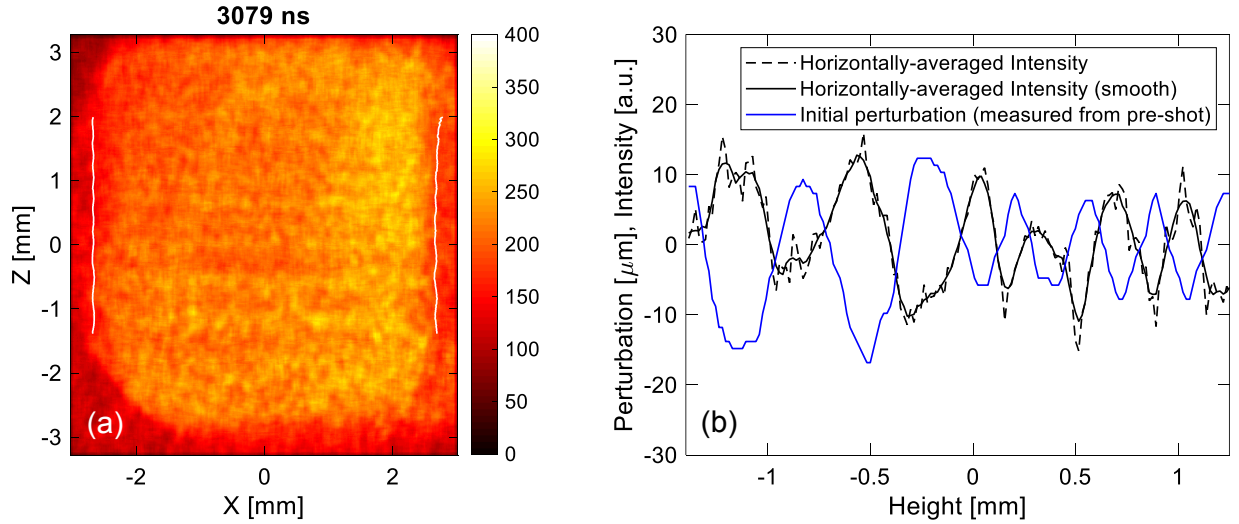

Figure 2-20. MRT Emission analysis

regions. This is consistent with current amplification theory, which predicts that current is concentrated in the bubble regions, causing these regions to ohmically heat more than the spike regions.[9]

2.6. MagLIF

SEGOI was also fielded on a MagLIF Current Scaling 20a experiment, z3564. The liner was obscured on the left and right sides by the return can and a diagnostic fiducial (TIPC), as shown in Fig. 2-21. In the figure, the dashed blue lines indicate the liner initial radius, and the blue boxes indicate the position of the cushions (obscured by load hardware). The diagnostic was fielded with varying gain settings, 200 ps gates and 6 ns interframe time. Throughout the frames, we see emission from the liner along with a dark region expanding

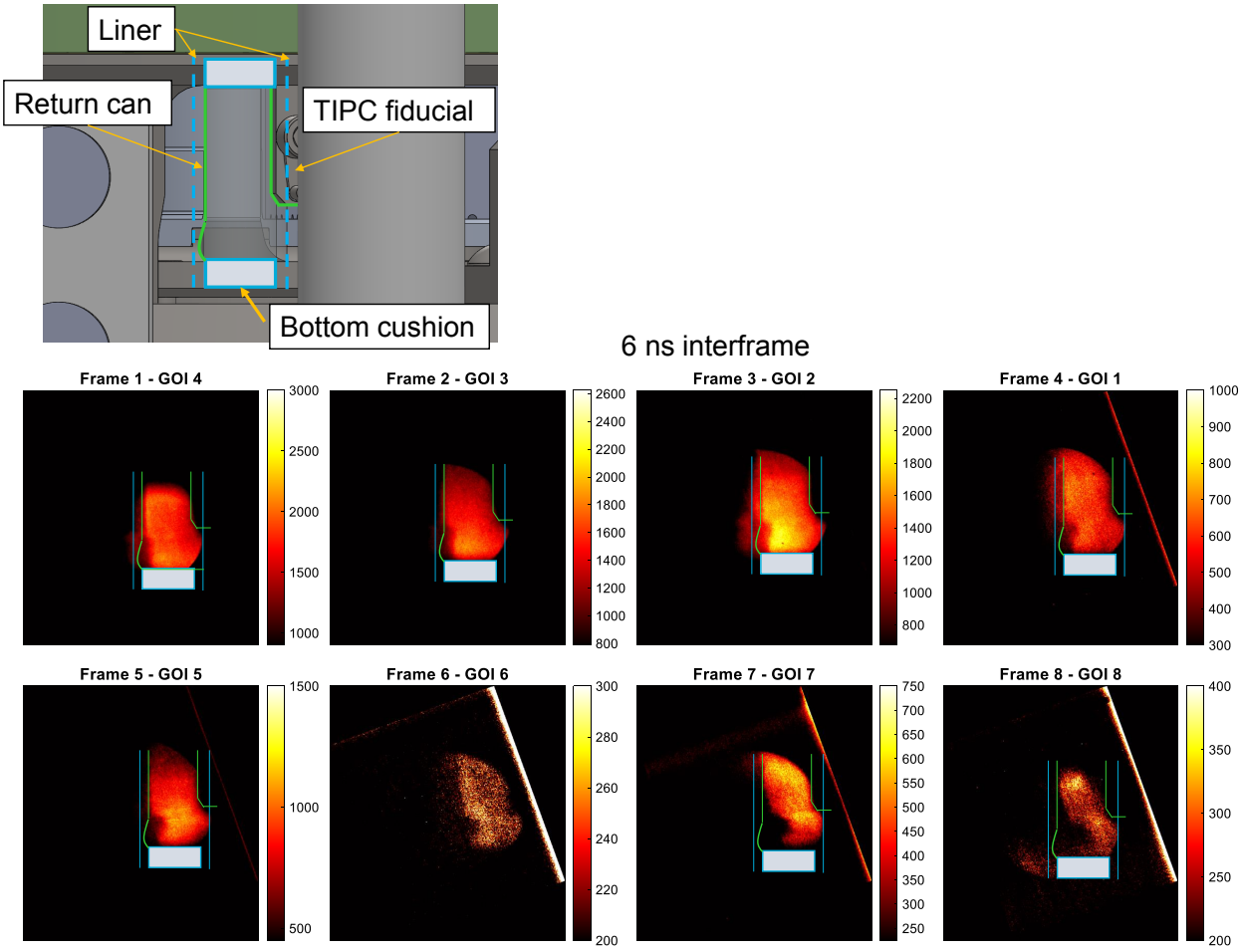

Figure 2-21. Top: Overview of target region viewed by SEGOI. The initial liner boundary is obscured by the return can and the TIPC fiducial. Bottom: Time-sequence of SEGOI images.

on the lower left of the target, above the cushion. This dark region is likely due to plasmas expanding from the return can. As we have seen, these plasmas are sufficiently opaque to block emission from the liner. This structure was initially attributed to the wall instability that forms at the liner-cushion boundary; however, by frame-7 it has extended beyond $R = 0$ with no corresponding bubble on the right side, indicating this explanation is nonphysical.

To be useful for MagLIF, this diagnostic should be fielded on the so-called "standard-feed", which offers significantly more diagnostic access compared to the "DTC-feed" fielded on z3564. In this configuration, the return can consists of discrete posts that do not obscure view of the target. This will provide a better opportunity to image the edges of the system while reducing both vignetting and plasma occlusion caused by the nearby structures.

2.7. Conclusions

To date, SEGOI has been fielded on four different experimental campaigns and a total of six Z experiments. The diagnostic has proven to be well-suited for imaging a variety of phenomenon, including the dynamics of low density plasmas on and expanding from transmission line surfaces, from ICF targets and return cans, for tracking liner implosion trajectories and for determining the relationship between perturbations on targets and their resulting emission structures. As with any new diagnostic, there is uncertainty in the proper settings for a given system; many of the frames acquired for these first experiments were too dim or saturated to be useful. Additionally, the four experiments were vastly different, ranging from imaging of AK gaps at large radii to beryllium and aluminum liners at currents from 14 to 20 MA. Despite this, with each experiment we gain more insight into the system and the emission of these targets, which guides us to better-informed diagnostic settings and ultimately higher quality data.

Beyond the Power Flow and ICF programs, SEGOI has been requested on a radiation effects science platform (CHIMP) to image plasma expansion from targets driven by intense radiation, and a Z fundamental science platform (MARZ) to image interactions of low density plasmas produced from an inverse wire-array with an obstruction. With modest improvements to the optical configuration of the GOIs and to the in-chamber diagnostics, SEGOI has the capability to provide greater impact across our center.

3. OPTICAL IMAGING OF THE POST-SHOT DEBRIS ENVIRONMENT

3.1. Introduction

The Z Machine delivers a tremendous amount of energy to the load hardware and targets, ultimately causing the target and parts of the load hardware to explode. This debris can be extremely destructive, damaging diagnostics, the insulator stack, and radiation effect sciences cassettes. Understanding the post-shot debris environment is important for improving the design of diagnostics and debris limiters, including the so-called "speed bumps," in the transmission lines on Z today. The implications of debris are even more important for a next-generation pulsed power machine, where significantly more energy will be delivered to the targets and surrounding load hardware. How do the mass and velocity of the debris scale with energy delivered to the target? Is energy delivered to the target the correct metric for scaling, or is there a better metric (e.g. peak current)? Answering these questions is critical for ensuring we can reliably design blast-shields and protect diagnostics, vacuum chambers, ports, and insulator stacks on a next generation facility.

Our present understanding of debris is based on visual inspection of debris damage and Debris Time of Flight (DToF) accelerometer data. DToF consists of two accelerometers radially separated in space. An understanding of the velocity of the debris is obtained by correlating signals between the two accelerometers. Presently, our leading hypothesis is that the debris evolves over four stages, including: (1) hot plasma from the target and surrounding load hardware; (2) molten spray; (3) shrapnel (e.g. "bullets"); and (4) large, slow moving fragments of the target assembly. Molten spray, which is a combination of liquid- and solid-state material is moving at about $\sim$40 m/s to $\sim$1 km/s and lasting up to 25 ms, is the most damaging type of debris. Figure 3-1 shows an overview of the debris, including an image from an alignment camera recording the debris inside the blast-shield during an experiment (the bright lines are fast-moving and heated bullets), an image of the damage to the load hardware after an experiment, and images of damage from molten spray and bullets.

Motivated by gaps in our understanding of how debris scales on Z, we designed a new in-chamber diagnostic called DINGOZ (Debris ImagiNG On Z). The purpose of the diagnostic is to acquire high-speed (e.g. 10-100 kfps) imaging data of the debris environment to understand the debris particulate volume (from cross-sectional data), velocity (from particle tracking), and spatial distribution. This data will ultimately be used to benchmark debris simulations, which can then be extrapolated to next-generation machines and also inform designs for new containment system architectures (on both Z and a next-gen machine).

Figure 3-1. Top left: Image from an alignment camera during a Z shot. Top right: Image of the damage to the load hardware following a Z experiment. Bottom: Aftermath of two types of debris, including molten spray (left) and bullets (right).

3.2. Diagnostic Design

To design DINGOZ, we teamed with the photometrics group (1535), who has extensive experience with fielding fast cameras in challenging conditions. The camera selected for this LDRD was a Phantom VEO 1310. To acquire a large FOV with best resolution, our major design requirement was that the camera be fielded in the center section. While future diagnostics could implement cameras outside of the chamber (e.g. in the interstitial space or Z boats), we desired a system that could image debris as close as possible. To accomplish this, we assembled a list of requirements:

Camera enclosure:

- Airbox system so the camera will be housed in a trapped atmospheric volume, required to operate and cool camera and to prevent batteries from outgassing.
- Aluminum walls 1/2 inch thick to protect components from debris
- Sufficiently large to house a variety of fast cameras (e.g. Phantom v2512) along with 3x batteries and electronics to trigger, power, and acquire data from camera
- Feedthrough ports for fibers and pressure lines
- Mounting fixtures to MITL (magnetically insulated transmission line) deck
- Appropriate fixtures for crane lift

Shock and Electromagnetic Interference (EMI) Isolation:

- Wire rope isolators to tamp high frequency oscillations from Z mechanical shock
- Enclosed metallic box to provide EMI shielding
- Battery-powered electronics to facilitate enclosure

Optics:

- Inner and outer 1/2 in thick polycarbonate windows to protect components from debris and to avoid replacing vacuum window on regular basis
- FOV of 0.5 - 1 m

The VEO camera is somewhat robust to mechanical shock (∼5-10 "g"s). However, the Z mechanical shock environment produces over 100 "g"s of shock, as measured on the MITL deck (see Fig. 3-2). Fortunately, this acceleration is experienced at high frequencies, making wire rope isolators an attractive option to limit the mechanical shock. Four wire rope isolaters were included in DINGOZ to damp this high frequency behavior. For a natural frequency of ∼1 Hz, the acceleration experienced is an acceptable 3 "g"s.

To minimize EMI, the system was designed to be battery powered. A significant effort was undertaken to understand the risks associated with batteries in the Z center section. As a part of this, we worked with Org. 7546 to identify batteries and risks. LiFePO4 batteries were identified as a promising option compared to other lithium batteries, with the major

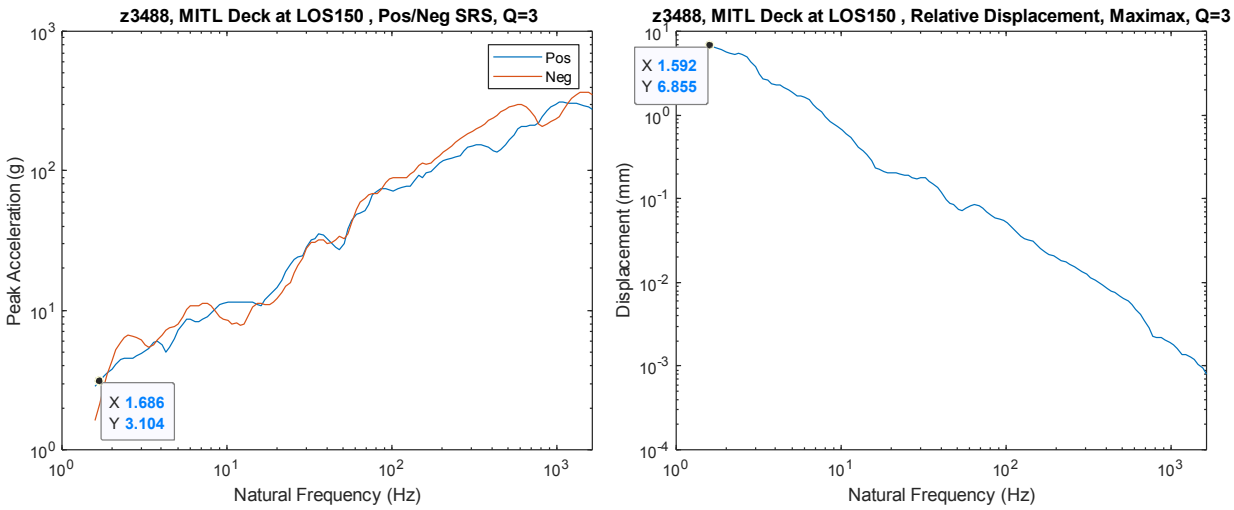

Figure 3-2. Accelerometer (left) and displacement (right) measurements as a function of frequency due to mechanical shock from a Z experiment.

risk being outgassing of volatiles due to the enclosure losing pressure (e.g. due to debris penetration). Previous experience with this type of battery showed the Z chamber was large enough that the purge (PSAX) cycle would be sufficient to eliminate the majority of volatiles from potentially damaged batteries. Our analysis concluded that, in the case pressure was lost in the enclosure, a second PSAX cycle would be recommended (but not required).

To maintain a pressurized enclosure (required for the camera, camera cooling, and batteries) we implemented O-rings into the design. However, a solution was required to demonstrate the air-tight system prior to Z installation. To resolve this, we over-pressurized the system by 3 PSIg (15 PSIa in Albuquerque) and monitored the leak-rate over a specified time. Calculations showed a 0.14 PSI decrease in pressure (from a 3 PSI differential) corresponds to a 0.7 PSI drop in the Z chamber when under vacuum (15 PSI differential), as shown in Fig. 3-3. This decrease in pressure is measurable over the course of one hour, and is sufficient to determine the readiness of DINGOZ for installation into the Z vacuum chamber.

An overview of the DINGOZ enclosure is shown in Fig. 3-4. The figure shows the various components, including the baseplate with wire-rope isolators, the lifting features, the primary debris shield, the periscope, the feedthrough port, and the metallic chassis. A top-down view of DINGOZ components and hardware is shown in Fig. 3-5. Also included in the figure is a rendering of DINGOZ on the MITL deck and an image of DINGOZ during commissioning.

A local network is created inside of DINGOZ by connecting the camera and x420 "Control By Web" system to the Trendnet ethernet switch and media converter. A laptop in the control room connects to a second Trendnet via an ethernet cable. Fiber optics connect the two Trendnets (fed-through the Z chamber and the DINGOZ enclosure), and allows the laptop to communicate with the x420. The electronics diagram is shown in Fig. 3-6. The x420 controls the power circuit via a web-interface for the camera (shown in Fig. 3-7) while

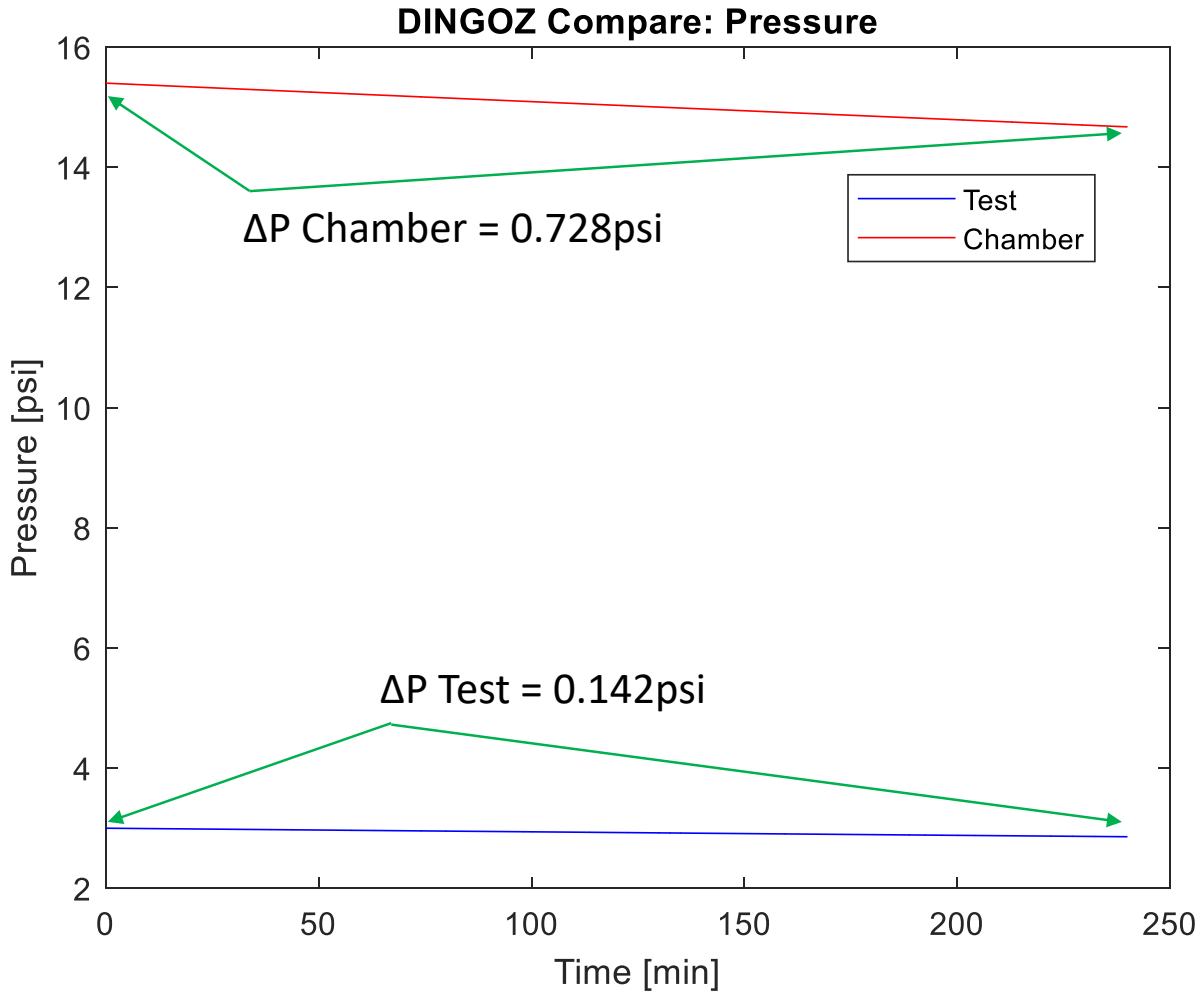

Figure 3-3. Pressure leak calculations for 25 μm diameter leak on Z (15 PSI differential) and at atmospheric pressure (3 PSI differential).

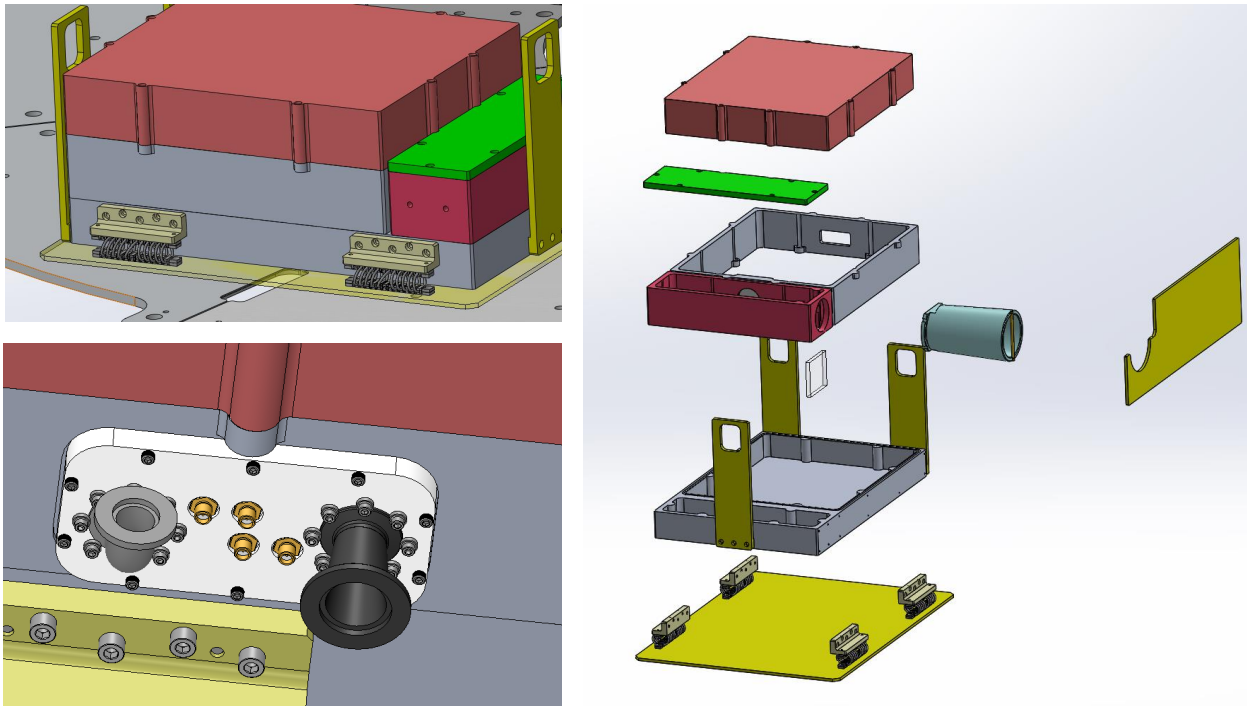

Figure 3-4. Images of the DINGOZ hardware and feedthrough ports.

recording the pressure inside the enclosure via a pressure transducer. When the camera is powered on, the laptop communicates to the camera via the Phantom Software.

The camera is triggered as follows. A delay generator in the control room is configured to send a voltage pulse to an electrical-to-optical converter. This optical signal is carried by a single fiber to the Z chamber and fed-through to the DINGOZ enclosure. Inside the enclosure, the optical signal is converted to an electrical signal that is used to trigger the camera. In practice, this signal is weak (due to the large fiber run and multiple fiber-connections). If even the camera cannot be triggered by this signal, an option is to trigger the camera manually. This may seem counter-intuitive, but exploits the continuous buffer signal recorded by the camera. After the Z shot, triggering the camera via software allows the camera to save images from a specified duration before the trigger event. As an example, the camera can be configured to store the 3 seconds of data before the triggering event and 1 second of data after the triggering event.

3.3. MagLIF Coil imaging at SITF

DINGOZ was tested at SITF (Systems Integration Test Facility) prior to commissioning on Z. One of the objectives of SITF is to test Helmholtz-like coils that are used for MagLIF experiments. These coils pulse on a ms-timescale and are well-suited targets for imaging by high-speed cameras.

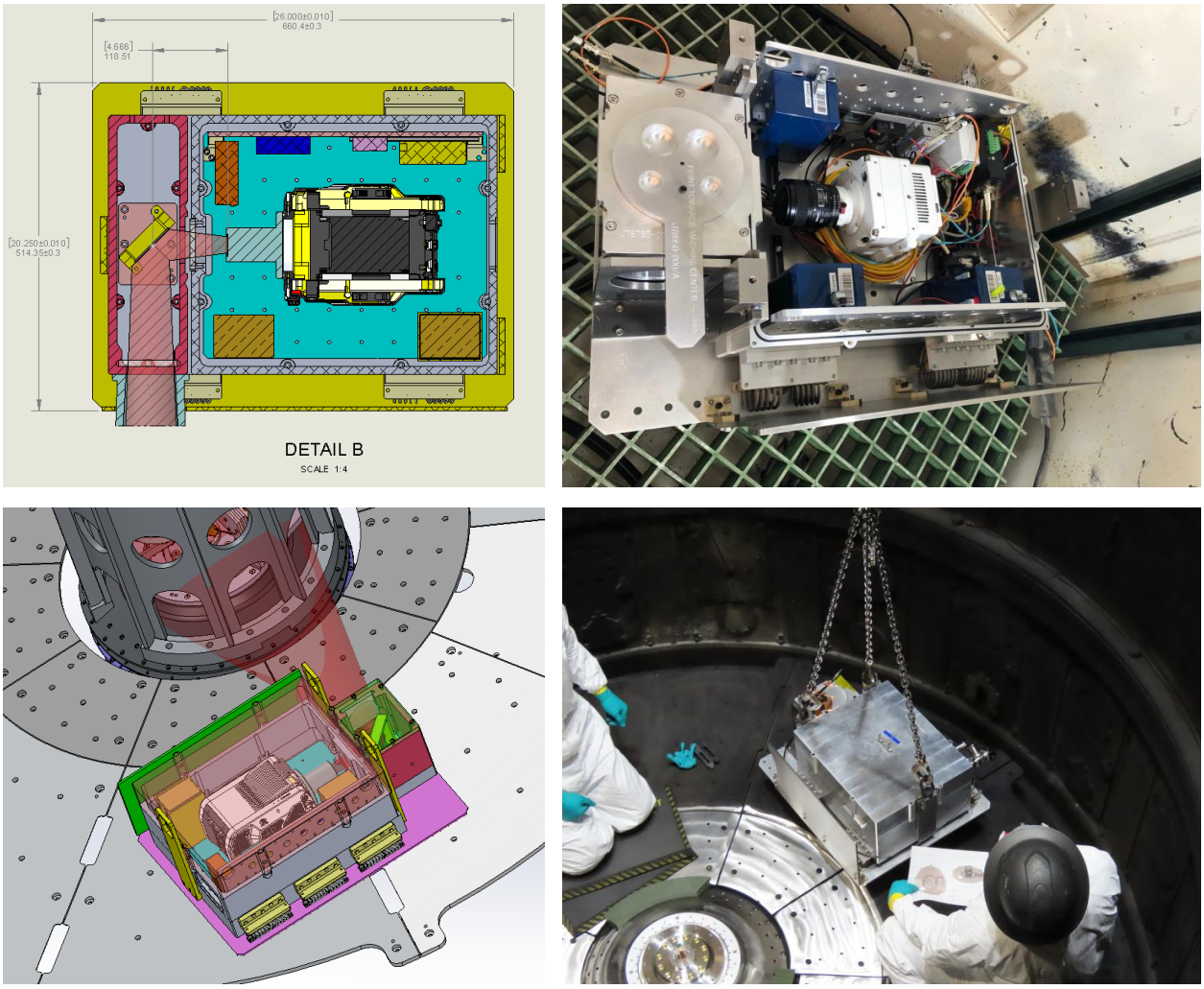

Figure 3-5. Images of the DINGOZ system fielded at SITF and on Z.

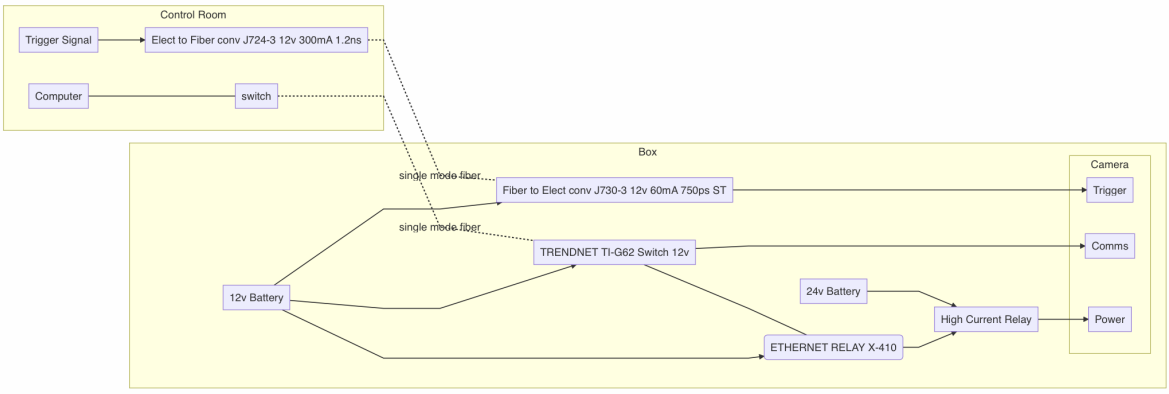

Figure 3-6. Electronics for DINGOZ system, including trigger and communications circuits.

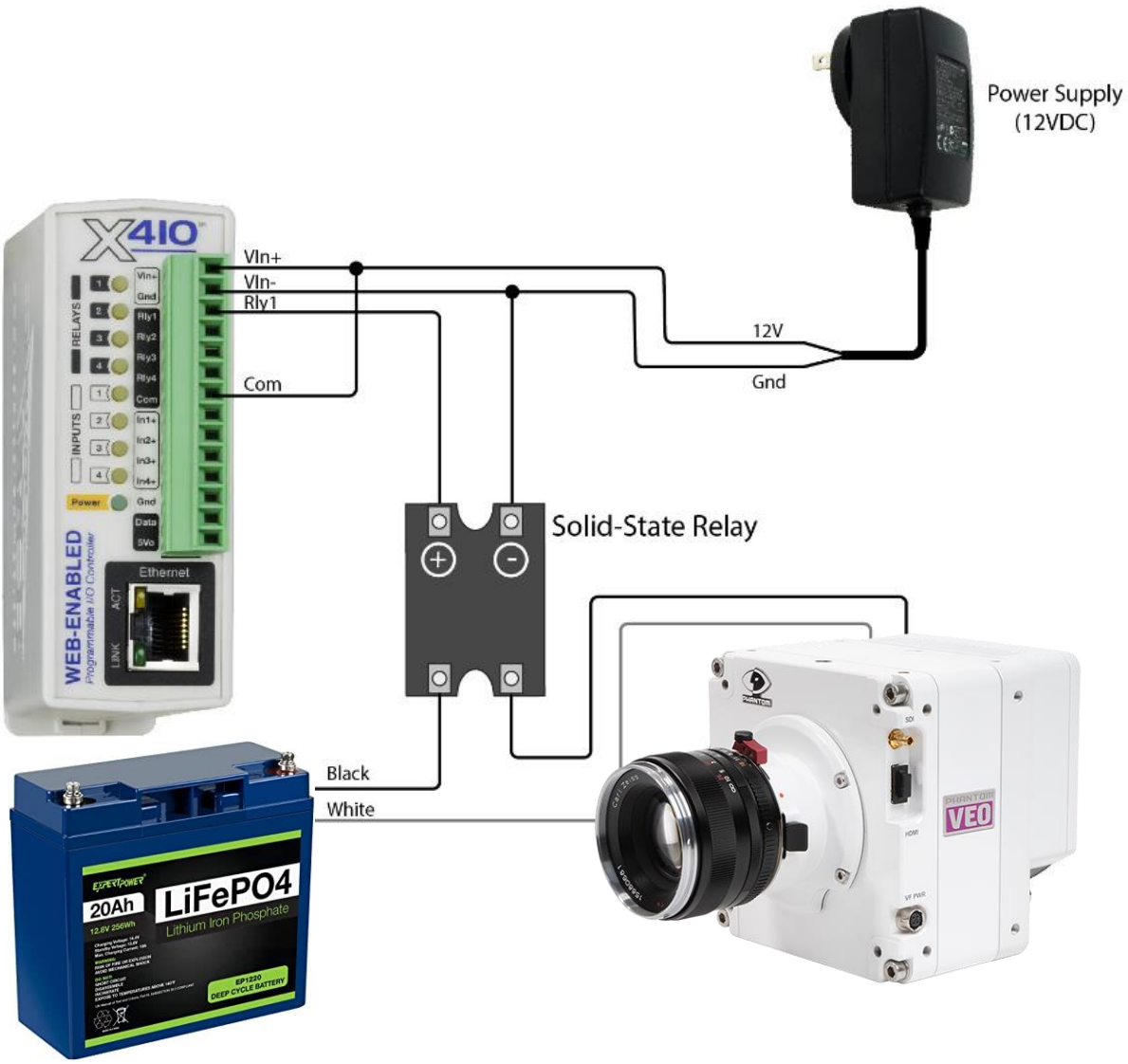

Figure 3-7. DINGOZ power circuit. The x420 (x410 shown in image) controls a high current relay that powers the camera via a LiFePO4 battery. In DINGOZ, the 12 V that powers the x420 is provided by an additional dedicated LiFePO4 battery.

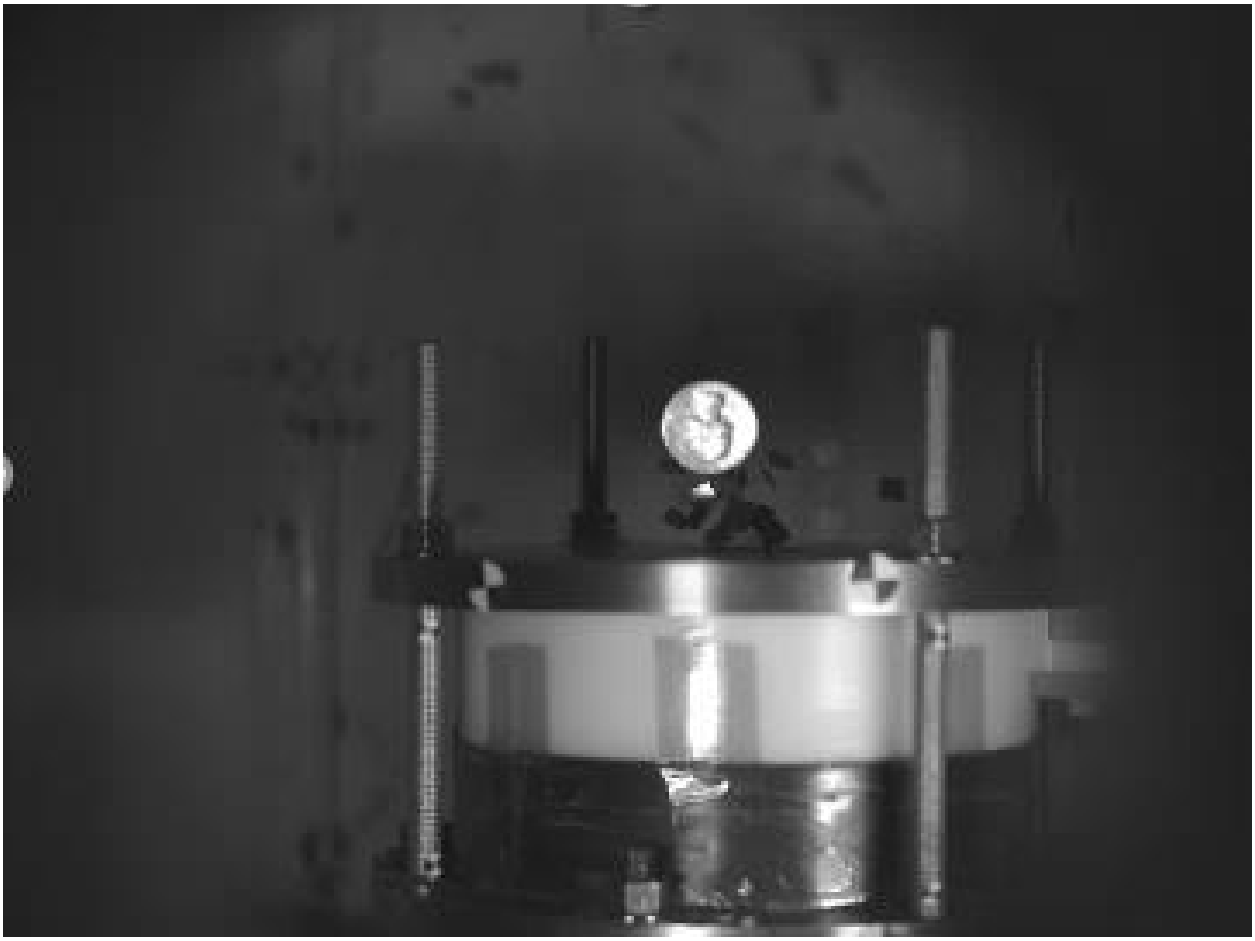

Figure 3-8. Image taken during a MagLIF coil pulse at SITF. Metallic objects are swept towards the Z axis, an observation with implications for dust particulate above the coils on MagLIF. This dust could interfere with the preheat laser and ultimately degrade target performance.

We acquired multiple videos of coils pulsing at 5 kV and 10 kV charge voltages. The videos showed small a deflection in the coil housing due to the large magnetic pressures generated. To image faster moving objects, we scattered a variety of small, rectangular foils on the top of the coil along with a single US quarter. As the coils were pulsed, the time-changing magnetic pressure drove the metallic components towards the Z-axis of the coils, as shown in Fig. 3-8. This observation is concerning for MagLIF, as we demonstrated any small metallic particulate could be swept towards the target Z-axis, interfering with the preheat laser. In fact, dust particulate have been observed above MagLIF targets during the preheat phase. These shots have a significantly degraded yield. In the future, fast framing cameras such as the VEO 1310 could be used to assist in failure mode testing of coils at SITF.

3.4. Debris Environment on 65 kV DMP Experiment

On the day prior to commissioning, we fielded DINGOZ on the Z mezzanine in ride-along mode to ensure it could trigger in the EMI environment. This test was successful, and on the following day (December 2nd, 2020) we commissioned DINGOZ on shot z3560 (Fe Strength in the Dynamic Material Properties program). This experiment was led by Justin Brown and Jean-Paul Davis and utilized a 65 kV charge voltage with asynchronous Marx bank triggering for pulse shaping.

DINGOZ was successfully triggered and acquired the first ever high-speed imaging data of the post-shot debris environment. Unfortunately, the DINGOZ camera was focused on the back chamber wall and not the blast-shield; therefore, the majority of the debris observed is out of focus (we have since acquired a remotely controlled focusing lens to prevent this issue from occurring). An image covering the camera layout in the MITL deck (along with camera parameters), generated using the Photometrics Calculator software, is shown in Fig. 3-9.

The camera was fielded with 250 μs interframe time. In Fig. 3-10, we show example frames covering the evolution of the debris over 130 ms after the Z pulse. The top-left image shows a pre-shot image. The illumination source was weak; however, the back chamber wall is in focus and the MITL deck and blast-shield are identifiable. Immediately following the Z shot the camera is fully saturated, likely by a combination of hot plasma and neutral gas. This light source decays in time, ceasing around 30 ms after the event. During this time, debris particulate are observed streaming out of the top and bottom blast-shield openings (see arrows in image at 37 ms). Debris continues to stream out of the blast-shield for around 100 ms, after which the emission is too weak to be detected by the camera.

Throughout the movie we see debris particulate that are in focus. Some of these are traveling left-to-right, indicating they have bounced off the chamber walls. These particles were tracked using the 1535 Photometrics group particle tracking software. Two frames of data are shown (33 ms in Fig. 3-11 and 155 ms in Fig. 3-12). Early in time we see relatively slow-moving debris particulate, with particles moving both left-to-right (particles 0, 1, and 8) and right-to-left (particles 57 and 68). The velocity of these debris particulate are all close to 30 m/s. In the figure, the trajectory of the particles is shown in red. Examining particle 68's trajectory, we see it is not perfectly smooth, with oscillations that start around 44 ms. The origin of these oscillations is likely due to pressure waves that have formed in the neutral gas that has filled the chamber following the explosion of the target and load hardware. Later in time at 155 ms we see more chaotic trajectories. Around this time, another pressure wave forms that oscillates most of the tracked particles. The exact origin of the waves are unknown. By this time, most particulate have slowed by a factor of 10, with most velocities less than 10 m/s. Interestingly, particle 1457 has a fast velocity of 23.9 m/s, comparable to the particles in the early time image. This could indicate continuous explosion of load hardware material; however, cleaner data must be acquired to confirm this.

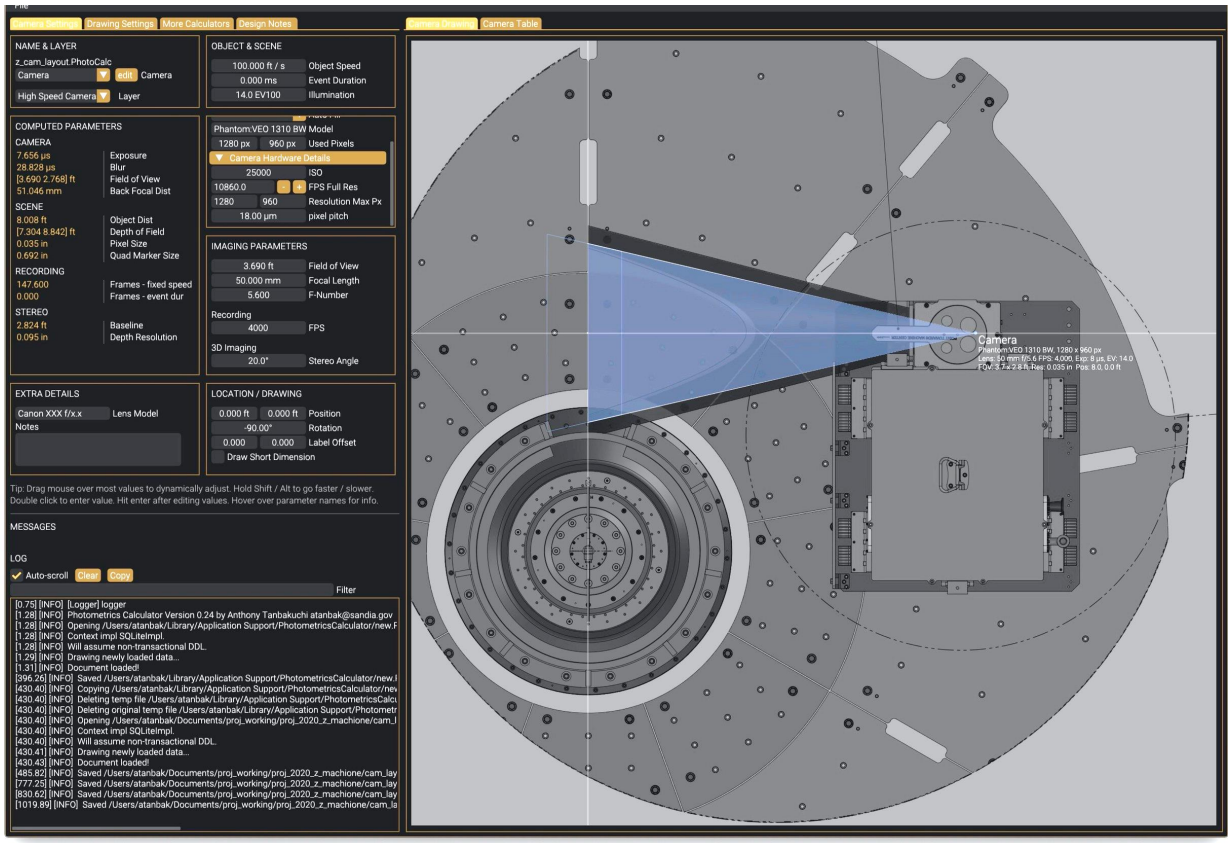

Figure 3-9. Photometrics calculator setup

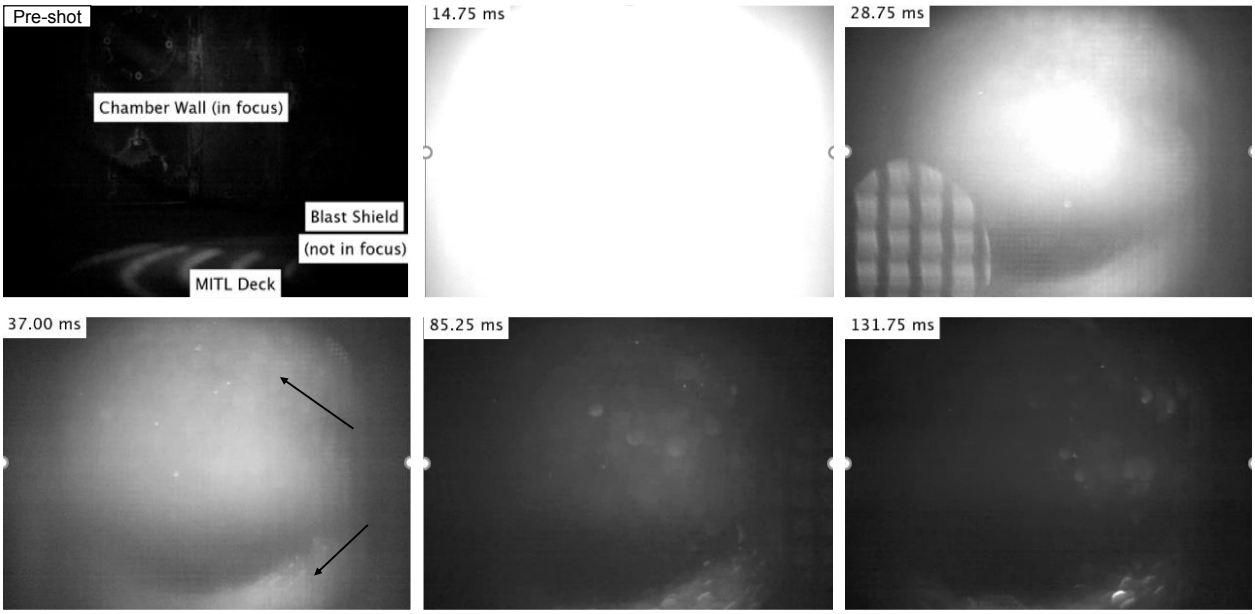

Figure 3-10. Data from 65 kV DMP experiment

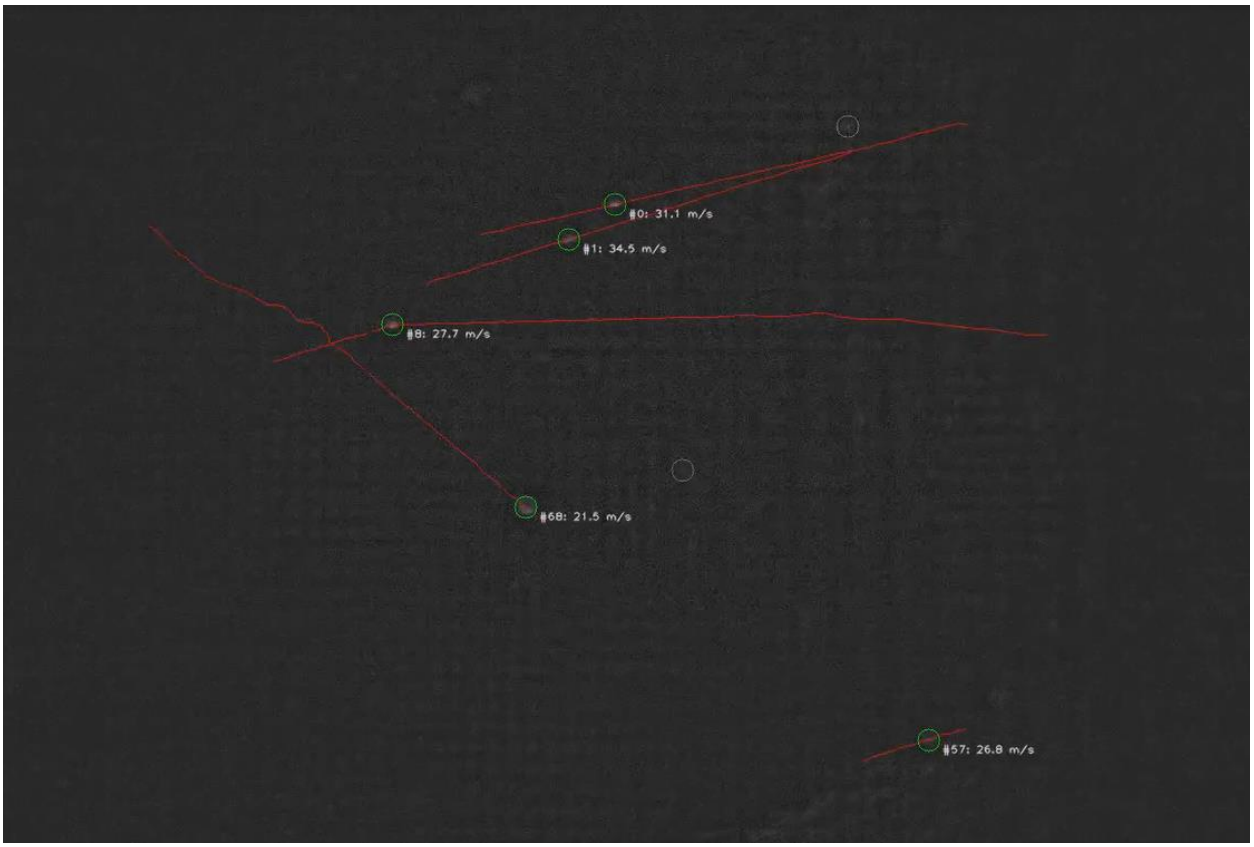

Figure 3-11. Tracking of debris particles early time (33 ms).

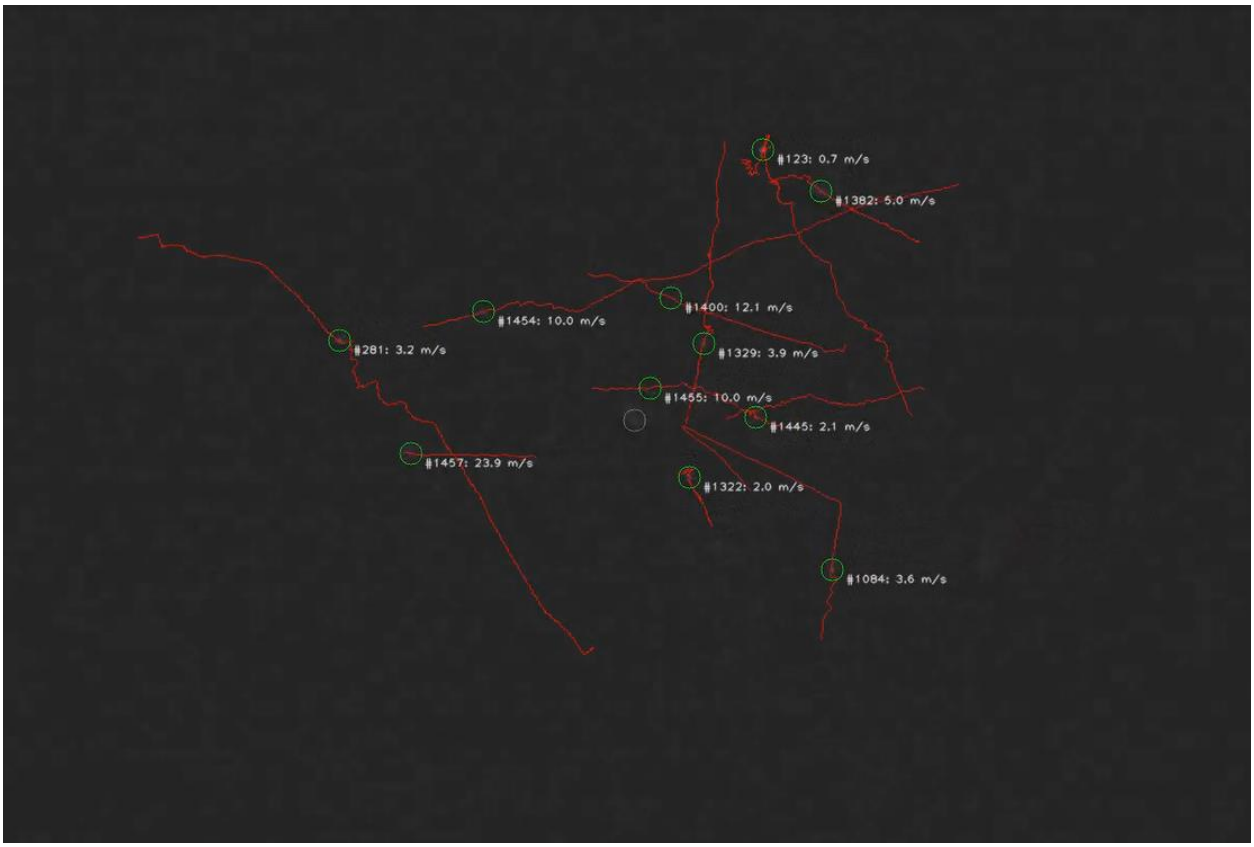

Figure 3-12. Tracking of debris particles late time (155 ms).

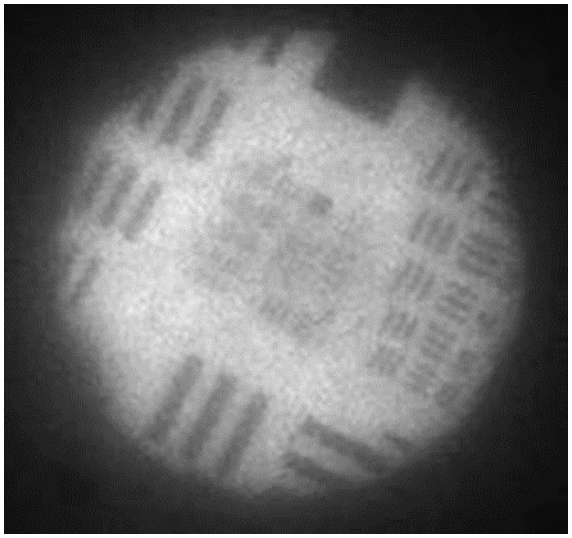

Figure 3-13. Image of resolution target acquired using FIZ and the VEO 1310 camera.

3.4.1. Subsequent DINGOZ attempts and upgrades

DINGOZ was fielded on 3 shots following the 65 kV DMP experiment. The first was a 90 kV DMP experiment. During the shot, the EMI environment disrupted the electronics and prevented the camera from acquiring data. At this time, the exact failure mechanism was unknown. Subsequent experiments on 85 kV short pulse Ramsey (an RES platform) experiments also caused electronics failures during the Z shots; however, close monitoring isolated the problem to the x420 Control by Web relay. The webpage attempted to refresh immediately following the Z shot and was unable to be found, indicating the x420 had experienced an intermittent failure and reset. Upon reset, the positive voltage applied to the high current relay switch is dropped, opening the camera power circuit and therefore turning off the camera. To address this, we teamed with 1536 to develop a backup power source for the camera. The source is a super-capacitor that outputs sufficient voltage and current to power the camera for ∼10 seconds following reset of the x420. Based on previous Z experiments, we expect this is more than sufficient time to manually reset the x420 voltage output to re-apply power to the camera. This solution has been tested offline and will be implemented on our next fielding opportunity.

3.4.2. Fiber Imaging on Z

In the final months of the LDRD, our team was introduced to a new fiber imaging capability developed by K. W. Fulford, a graduate student intern from the University of New Mexico, and S. Patel (1659). This type of imaging utilizes a single high resolution PMMA fiber optic cable (i.e. a single fiber with 13,000 fused fiber cores), allowing images to be acquired and relayed long distances without mirrors. The diagnostic is called Fiber Imaging on Z (FIZ).

Fiber imaging is extremely versatile. In essence, an image is formed on the ∼2 mm OD fiber front-end via a lens and transported to an image collection system that images the light output of the fiber. Therefore, the front-end lens determines the image properties (e.g. FOV and resolution). Previously, Fulford and Patel demonstrated as high as 3 μm resolution using this system. For this project, the team adapted FIZ to view the post-shot debris environment by fitting a wide-angle lens to the front-end and designing a COTS mounting bracket that fixes the fiber and lens to the top of the blast-shield. This allows FIZ to acquire images of the post-shot debris exploding out of the blast-shield. The fiber is relayed to the LOS30 screenbox and imaged onto the VEO 1310 camera. An image of a resolution target is shown in Fig. 3-13, showing a FOV of 45 mm and resolution of 630 μm. A rendering of the FIZ mounting structure and load hardware is shown in Fig. 3-14.

FIZ was fielded on the Debris Shield Assessment Shot 21a on September 8th, 2021. Unfortunately, this shot experienced a pre-fire in the Marx Trigger Generator and no usable data was acquired on the shot. Future experiments incorporating FIZ in debris monitoring mode are planned later in CY2021.

3.5. Additional Impacts

DINGOZ demonstrated it is possible to field an atmospheric enclosure in the Z center section and isolate the components from Z's mechanical shock. In a planned ride-along test, the DINGOZ enclosure will be used to house a battery powered digitizer. If the digitizer is successfully triggered, the follow-on plan is to field a pyrometry diagnostic to measure infrared light via fiber optic. This capability would significantly reduce the cost in consumables compared to a system using a digitizer external to Z as the pyrometry fibers are extremely expensive.

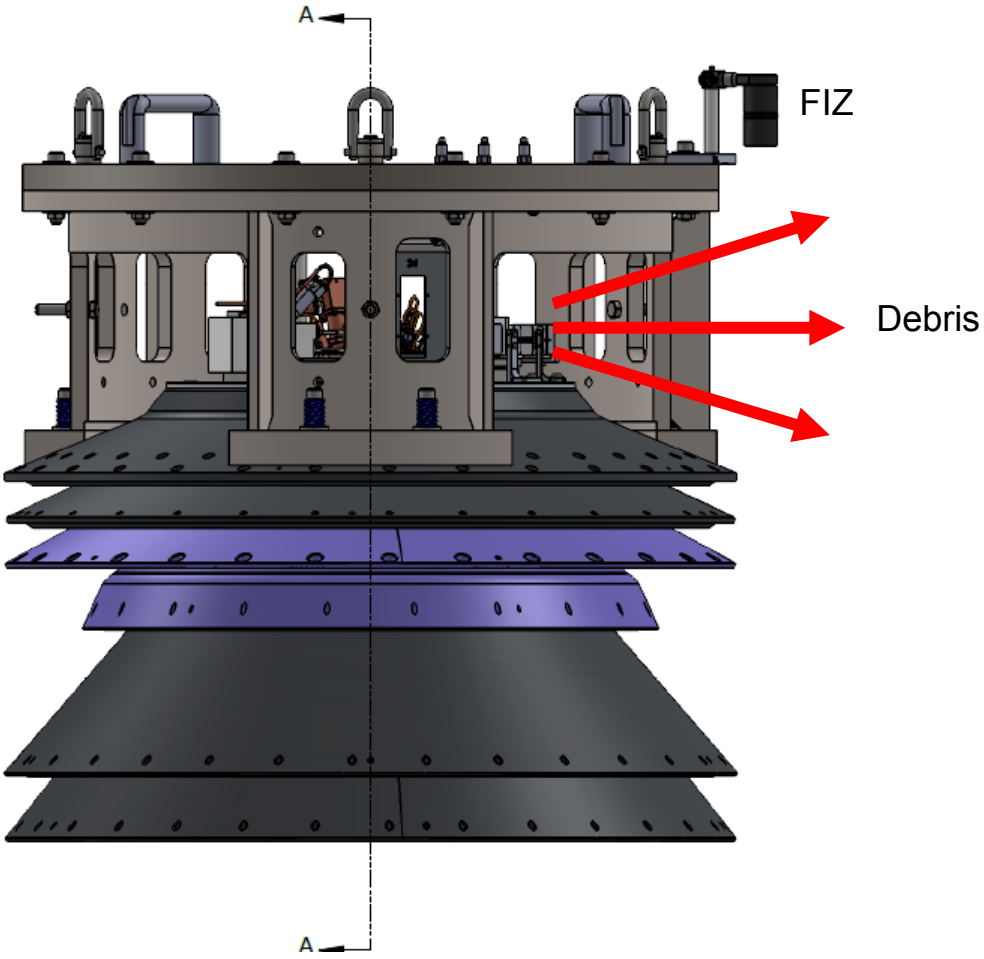

Figure 3-14. Adaptation of FIZ to image the post-shot debris environment. FIZ is mounted to the top of the blast-shield and images top-down.

4. CONCLUSIONS

In this LDRD we have developed two new diagnostics, SEGOI and DINGOZ, and adapted one diagnostic, FIZ, for imaging optical phenomenon on Z, including emission from low density plasmas and from the post-shot debris environment.

SEGOI enabled high quality 1 and 2D imaging data of plasmas produced on transmission line surfaces, between helical return current posts on the dynamic screw pinch platform, on the surfaces of targets designed to measure the magneto Rayleigh-Taylor instability, and on Magnetized Liner Inertial Fusion targets. We have presented a preliminary analysis of the phenomenon and identified its significance. SEGOI will be an impactful diagnostic moving forward and has been requested across four 1600 programs including ICF, Power Flow, RES, and Z Fundamental Science.

DINGOZ enabled the first high-speed images of the post-shot debris environment, acquired by an in-chamber camera protected in an air-tight enclosure. This diagnostic will be utilized moving forward to improve our understanding of the post-shot debris environment and, in particular, to understand the scaling relationship between debris mass and velocity and driver energy.

FIZ was adapted from a fiber imaging diagnostic designed by K. W. Fulford and S. Patel in order to image the post-shot debris environment. This diagnostic has been fully developed and will be applied to experiments following the conclusion of this LDRD.

REFERENCES

[1] M. E. Savage, K. LeChien, W. Stygar, J. Maenchen, D. McDaniel, and K. Struve, Proceedings of the 2008 IEEE International Power Modulators and High Voltage Conference p. 93 (2008).

[2] A. Porwitzky, D. Dolan, M. R. Martin, G. Laity, R. Lemke, and T. R. Mattsson, Physics of Plasmas **25**, 063110 (2018).

[3] P. Datte, J. Baker, D. Bliss, N. Butler, P. Celliers, S. Cohen, M. Crosley, J. Edwards, D. Erskine, D. Fratanduono, et al., Review of Scientific Instruments **91**, 043508 (2020).

[4] P. Schmit, A. Velikovich, R. McBride, and G. Robertson, Physical review letters **117**, 205001 (2016).

[5] G. A. Shipley, C. A. Jennings, and P. F. Schmit, Physics of Plasmas **26**, 102702 (2019).

[6] P. C. Campbell, T. Jones, J. Woolstrum, N. Jordan, P. Schmit, J. Greenly, W. Potter, E. Lavine, B. Kusse, D. Hammer, et al., Physical Review Letters **125**, 035001 (2020).

[7] D. B. Sinars, S. A. Slutz, M. C. Herrmann, R. D. McBride, M. E. Cuneo, K. J. Peterson, R. A. Vesey, C. Nakhleh, B. E. Blue, K. Killebrew, et al., Phys. Rev. Lett. **105**, 185001 (2010).

[8] D. B. Sinars, S. A. Slutz, M. C. Herrmann, R. D. McBride, M. E. Cuneo, C. A. Jennings, J. P. Chittenden, A. L. Velikovich, K. J. Peterson, R. A. Vesey, et al., Phys. Plasmas **18**, 056301 (2011).

[9] E. P. Yu, T. J. Awe, K. R. Cochrane, K. C. Yates, T. M. Hutchinson, K. J. Peterson, and B. S. Bauer, Physics of Plasmas **27**, 052703 (2020).

DISTRIBUTION

Hardcopy—Internal

Number of Copies	Name	Org.	Mailstop
1	David A. Yager-Elorriaga	1683	1193

Email—Internal [redacted]

Name	Org.	Sandia Email Address
Technical Library	01177	libref@sandia.gov

Sandia National Laboratories is a multimission laboratory managed and operated by National Technology & Engineering Solutions of Sandia LLC, a wholly owned subsidiary of Honeywell International Inc., for the U.S. Department of Energy's National Nuclear Security Administration under contract DE-NA0003525.